

Article

Synthesis of High-Input Impedance Electronically Tunable Voltage-Mode Second-Order Low-Pass, Band-Pass, and High-Pass Filters Based on LT1228 Integrated Circuits

Hua-Pin Chen , Shih-Jun Chen and Chih-Yang Chang

Department of Electronic Engineering, Ming Chi University of Technology, Taipei 24301, Taiwan

* Correspondence: hpchen@mail.mcut.edu.tw; Tel.: +886-2-2908-9899; Fax: +886-2-2908-5247

Abstract: This paper introduces two new high-input impedance electronically tunable voltage-mode (VM) multifunction second-order architectures with band-pass (BP), low-pass (LP), and high-pass (HP) filters. Both proposed architectures have one input and five outputs, implemented employing three commercial LT1228 integrated circuits (ICs), two grounded capacitors, and five resistors. Both proposed architectures also feature one high-impedance input port and three low-impedance output ports for easy connection to other VM configurations without the need for VM buffers. The two proposed VM LT1228-based second-order multifunction filters simultaneously provide BP, LP, and HP filter transfer functions at V_{o1} , V_{o2} , and V_{o3} output terminals. The pole angular frequencies and the quality factors of the two proposed VM LT1228-based second-order multifunction filters can be electronically and orthogonally adjusted by the bias currents from their corresponding commercial LT1228 ICs, and can be independently adjusted in special cases. In addition, both proposed VM LT1228-based second-order multifunction filters have two independent gain-controlled BP and LP filter transfer functions at V_{o4} and V_{o5} output terminals, respectively. Based on the three commercial LT1228 ICs and several passive components, simulations and experimental measurements are provided to verify the theoretical predictions and demonstrate the performance of the two proposed high-input impedance electronically tunable VM LT1228-based second-order multifunction filters. The measured input 1-dB power gain compression point (P1dB), third-order IMD (IMD3), third-order intercept (TOI) point, and spurious-free dynamic range (SFDR) of the first proposed filter were -7.1 dBm, -48.84 dBc, 4.133 dBm, and 45.02 dBc, respectively. The measured input P1dB, IMD3, TOI, and SFDR of the second proposed filter were -7 dBm, -49.65 dBc, 4.316 dBm, and 45.88 dBc, respectively. Both proposed filters use a topology synthesis method based on the VM second-order non-inverting/inverting HP filter transfer functions to generate the BP, LP and HP filter transfer functions simultaneously, making them suitable for applications in three-way crossover networks.



Citation: Chen, H.-P.; Chen, S.-J.; Chang, C.-Y. Synthesis of High-Input Impedance Electronically Tunable Voltage-Mode Second-Order Low-Pass, Band-Pass, and High-Pass Filters Based on LT1228 Integrated Circuits. *Sensors* **2022**, *22*, 9379. <https://doi.org/10.3390/s22239379>

Academic Editors: Serioja Ovidiu Tatu and Youfan Hu

Received: 31 October 2022

Accepted: 30 November 2022

Published: 1 December 2022

Publisher's Note: MDPI stays neutral with regard to jurisdictional claims in published maps and institutional affiliations.



Copyright: © 2022 by the authors. Licensee MDPI, Basel, Switzerland. This article is an open access article distributed under the terms and conditions of the Creative Commons Attribution (CC BY) license (<https://creativecommons.org/licenses/by/4.0/>).

Keywords: filters; analog circuit design; integrated circuit; commercial LT1228

1. Introduction

Electronically tunable active filters and oscillators designed with active components are widely used in sensor applications such as electrocardiography systems [1], biosensors [2], electronically tunable LC oscillators [3], and phase-sensitive detection [4]. Especially in the electronic sensor systems, electronically tunable active filters are used to filter out noise in the sensor systems [5]. An interesting dual-output MOSFET-only filter without any passive components is also presented in [6]. It has proven to be an effective solution for high frequency ranges. Electronically tunable voltage-mode (VM) high-pass filter (HPF), band-pass filter (BPF), and low-pass filter (LPF) topologies suitable for integrated circuit (IC) structures have been a constant endeavor of circuit designers, and have become very important architecture circuits in sensors, analog systems, electrical and electronic engineering works. The choice of active building blocks (ABBs) plays an important role in

analog filter design because one expects VM second-order multifunction filters with high input and low output impedances to allow cascading of the VM circuits. Therefore, many circuit architecture studies use different high-performance ABBs to implement different kinds of filters and oscillators [7–22]. In [22], a high-input impedance VM second-order filter based on four second-generation current conveyor (CCII) active components and six passive components is proposed. The filter can simultaneously implement LP, BP, HP, band-reject (BR), and all-pass (AP) filters from the same circuit configuration, but the filter lacks the low-output impedances. In [23,24], three current feedback amplifier (CFA) active components and six passive components are used in each VM second-order filter circuit design. The technique of [23,24] is implemented with three commercially available AD844 ICs, but neither the pole angular frequency (ω_o) nor the quality factor (Q) can be electronically adjusted. In [25], four CFA active components, seven/eight passive components, and one/two switches (SWs) are used in each VM second-order filter circuit design. Each circuit in [25] is implemented using four commercially available AD844 ICs, allowing four different filter responses simultaneously, but the parameters ω_o and Q of each circuit still cannot be electronically adjusted. In [26,27], three voltage differencing differential difference amplifier (VDDDA) active components and three passive components are used in the VM second-order filter circuit design. Each technology has the ability to electronically adjust ω_o and Q, enabling simultaneous implementation of LP, BP, HP, BR, and AP filters, but each circuit requires six commercial ICs to implement the VM filter architecture, namely three LM13700 and three AD830 ICs. In [28], two voltage differencing differential input buffered amplifier (VD-DIBA) active components and four passive components are used in the VM second-order filter circuit design. The circuit also has the ability to electronically adjust ω_o and Q, enabling simultaneous implementation of LP, BP, HP, and BR filters, but the circuit is implemented using four commercial ICs, namely two LM13700 and two AD830 ICs. Two electronically tunable VM second-order filters based on five operational transconductance amplifiers (OTAs) have been designed and developed [29,30], but these two configurations suffer from low-output impedance and the use of five LT1228 ICs. In [31], four OTAs and two grounded capacitors are used in the design of an electronically tunable VM second-order filter, but the technique is still implemented using five commercially available LT1228 ICs.

Due to its wide transconductance amplifier, high voltage-gain, large signal bandwidth, wide supply voltage, high accuracy, and high drive capability, the commercially available LT1228 IC is an interesting electronically tunable active component suitable for many circuit designs. As a result, many active VM second-order filters, oscillators, inductance simulators, and wave generators based on the attractive commercial LT1228 ICs were proposed in the literature [32–48]. The LT1228 implements gain-controlled through a transconductance g_m at the front end and a CFA at the back end, and combines these two amplifiers into an 8-pin package [49]. It operates on any supply voltage between 4 V (± 2 V) and 30 V (± 15 V) [49]. The LT1228's first-stage g_m transconductance amplifier has a high-impedance differential input pair and a high-impedance current output to provide a wide range of voltage-to-current conversion. The LT1228's second stage CFA has a low-output impedance and a wide voltage-gain range, making it ideal for driving low-impedance loads and avoiding loading effects. According to [32], two interesting independent amplitude VM BPFs are proposed, but both the HPF and LPF cannot be simultaneously obtained in each circuit configuration. The high-fidelity three-way speaker system uses one HPF, one BPF, and one LPF to connect the tweeter, midrange, and woofer, so the HPF, BPF, and LPF structures must be simultaneously implemented in the circuit design [31,33]. An interesting LT1228-based electronically tunable VM second-order multifunction filter is presented in [33], which simultaneously implements HPF, BPF, and LPF transfer functions from the same circuit configuration. According to [33], the circuit has the following features: (i) The filter can simultaneously generate VM second-order HPF, BPF, and LPF transfer functions, and is suitable for three-way crossover networks. (ii) The parameters of the filter, ω_o and Q, permit for electronic and orthogonal controllability. (iii) The HPF and BPF responses

provide low-output impedance, and can be directly cascaded to other VM circuits without the use of additional VM buffers.

In this paper, two new synthesis methods for VM LT1228-based second-order multifunction filters based on non-inverting/inverting HPF transfer functions are designed and developed. Each of the two proposed designed and synthesized VM second-order multifunction filters uses three commercial LT1228s, five resistors, and two grounded capacitors, which is one more resistor than the filter topology implemented in [33], to achieve two independent gain-controlled filter responses. Both the designed and the synthesized VM second-order multifunction filters have the following advantages.

- (i) The filter can simultaneously generate HPF, BPF, and LPF second-order transfer functions, and is suitable for three-way crossover networks.
- (ii) The parameters of the filter, ω_o and Q , permit for electronic and orthogonal controllability.
- (iii) The filter parameter Q has independent and electronic tuning capability.
- (iv) The filter provides a high-impedance input suitable for cascading voltage input stages.
- (v) The HPF, BPF, and LPF responses provide low-impedance outputs suitable for cascading voltage output stages.
- (vi) Passive components do not require matching conditions.
- (vii) The passband gains of the LPF and BPF responses can be controlled effectively and independently without affecting the filter parameters ω_o and Q .
- (viii) Synthesis methods of the filter topologies based on VM non-inverting/inverting HPF second-order transfer functions.

In addition to the three advantages (i) to (iii) realized in [33], these two new circuits provide the functions (iv) to (viii). In Table 1, the main characteristics of the two proposed LT1228-based electronically tunable VM second-order multifunction filters are compared with previous VM second-order multifunction filters implemented using commercially available ICs technology. As shown in Table 1, the two proposed LT1228-based electronically tunable VM second-order multifunction filters have independent gain-controlled LPF and BPF functions and satisfy all the main (i) to (viii) advantages. Both proposed filters use a topology synthesis method based on the VM second-order non-inverting/inverting HPF transfer functions to generate the BPF, LPF, and HPF transfer functions simultaneously, making them suitable for applications in three-way crossover networks [33]. To confirm the circuit performances of both proposed VM multifunction filters, PSpice simulation, measurement and theoretical calculation results are performed using three LT1228 ICs and several passive components.

2. Theory and Implementation of VM Second-Order Multifunction Filters Based on Non-Inverting/Inverting HPF Transfer Functions

2.1. First Proposed Synthesis Principle and Analysis Theory Based on Inverting HPF Transfer Function

To synthesize the first proposed VM second-order multifunction filter design system block, the VM inverting HPF (IHPF) second-order transfer function with two integrator time constants τ_1 and τ_2 and a voltage passband gain k_1 can be considered as the following function.

$$\frac{V_{\text{IHPF}}}{V_{\text{in}}} = \frac{-k_1 s^2}{s^2 + s \frac{k_1}{\tau_1} + \frac{1}{\tau_1 \tau_2}} \quad (1)$$

where V_{IHPF} is one of the output voltages of the first proposed filter, and V_{in} is the input voltage signal of the circuit.

To decompose the VM IHPF second-order transfer function into the VM non-inverting LPF (NLPF) and non-inverting BPF (NBPF) transfer functions, the terms of Equation (1) can be cross-multiplied first, and then divided by s^2 to obtain

$$V_{\text{IHPF}} = -\frac{k_1}{s\tau_1} V_{\text{IHPF}} - \frac{1}{s^2 \tau_1 \tau_2} V_{\text{IHPF}} - k_1 V_{\text{in}} \quad (2)$$

Table 1. Comparison of recent electronically tunable VM second-order multifunction filter specifications.

Ref.	ABB and Passive Elements Used		No. of Commercial ICs Realized	No. of Filtering Functions at the Same Time	No. of Low Output Impedance Filtering Functions Used	Only High-Input Impedance Used	Only Two Grounded Capacitors Used	Simultaneous Realization of Filtering Functions	Independent Gain-Controlled Filtering Functions	Orthogonal Electronic Control of Q and f_0	Independent Electronic Control Q without Affecting f_0	Q-Value or Q Tuning Range	Pole Frequency f_0 or f_0 Tuning Range (kHz)
	ABB	Passive											
[22]	4 CCII	2C + 4R	4	5	0	yes	yes	LPE, BPE, HPF, BRF, APF ^a	no	no	no	<5	15
[23]	3 CFA	2C + 4R	3	3	3	yes	yes	LPE, BPE, BRF	no	no	no	1.1–4	49–197
[24]	3 CFA	2C + 4R	3	3	3	yes	yes	LPE, BPE, HPF	no	no	no	0.6–1.6	86–170
[25]	4 CFA in filter 1a	2C + 5R + 2SW	4	4	4	yes	yes	LPE, BPE, BRF, HPF/APF	no	no	no	0.3–3.2	150
[25]	4 CFA in filter 1b	2C + 6R + 2SW	4	4	4	yes	yes	LPE, BPE, BRF, HPF/APF	no	no	no	<0.7	22–210
[25]	4 CFA in filter 1c	2C + 6R + 1SW	4	4	4	yes	yes	LPE, BPE, BRF, HPF/APF	no	no	no	0.3–3.3	22–210
[26]	3 VDDDA	2C + 1R	5	6	3	yes	yes	LPE, 2 BPE, HPE, BRF, APF	no	yes	yes	0.3–26.6	1047
[27]	3 VDDDA	2C + 1R	5	5	2	yes	yes	LPE, BPE, HPE, BRF, APF	no	yes	yes	1–4.5	625–1500
[28]	2 VD-DIBA	2C + 2R	4	4	2	yes	yes	LPE, BPE, HPE, BRF	no	no	no	2–5	66–144
[29]	5 OTA	2C	5	3	0	yes	yes	LPE, BPE, BRF	no	yes	yes	1–3	156–472
[30]	5 OTA	2C	5	3	0	yes	yes	LPE, BPE, BRF	no	yes	yes	1–2.9	107–284
[31]	4 OTA	2C	5	3	0	yes	yes	LPE, BPE, BRF	no	yes	yes	1–1.7	106–213
[32]	3 LT1228 in filter 2a	2C + 3R	3	3	2	yes	yes	3 BPF	1 BPF	no	no	1–2.9	161
[32]	3 LT1228 in filter 3a	2C + 3R	3	3	2	yes	yes	3 BPF	1 BPF	no	no	1–2.9	165
[33]	3 LT1228	2C + 4R	3	3	2	no	yes	HPF, BPE, LPF	no	yes	yes	0.4–1.7	100–373
[34]	2 LT1228 in filter 1	2C + 3R	2	3	2	no	yes	HPF ^a , BPF ^a , LPF ^a	no	no	no	<1.6	135–826
[34]	2 LT1228 in filter 2	2C + 3R	2	3	2	no	yes	HPF ^a , BPF ^a , LPF ^a	no	no	no	<1.6	44.3–275
[35]	2 LT1228 in filter 2a	2C + 5R	2	3	2	no	yes	HPF ^a , BPF ^a , LPF ^a	no	no	no	0.9–4.5	57–205
[35]	2 LT1228 in filter 2b	2C + 5R	2	3	2	no	yes	HPF ^a , BPF ^a , LPF ^a	no	no	no	0.9–4.5	99
Circuit 1	3 LT1228	2C + 5R	3	5	3	yes	yes	HPF, 2 BPE, 2 LPF	1 LPE, 1 BPF	yes	yes	0.7–6	46–961
Circuit 2	3 LT1228	2C + 5R	3	5	3	yes	yes	1 HPF, 2 BPE, 2 LPF	1 LPE, 1 BPF	yes	yes	0.7–6	46–879

Note: ABB: active building block; ^a requirements for resistor matching conditions.

Rearranging Equation (2) can be rewritten as

$$V_{\text{IHPF}} = \left(k_1 + \frac{1}{s\tau_2}\right) \left(-\frac{1}{s\tau_1}V_{\text{IHPF}}\right) - k_1V_{\text{in}} \quad (3)$$

Let

$$V_{\text{NBPF}} = -\frac{1}{s\tau_1}V_{\text{IHPF}} \quad (4)$$

This indicates that the NBPF signal can be achieved by cascading the IHPF signal with an inverting loss integrator, and Equation (3) becomes

$$V_{\text{IHPF}} = k_1V_{\text{NBPF}} + \frac{1}{s\tau_2}V_{\text{NBPF}} - k_1V_{\text{in}} \quad (5)$$

Let

$$V_{\text{NLPF}} = \frac{1}{s\tau_2}V_{\text{NBPF}} \quad (6)$$

This means that the NLPF signal can be achieved by cascading the NBPF signal with a non-inverting loss integrator, and Equation (6) becomes

$$V_{\text{IHPF}} = k_1V_{\text{NBPF}} + V_{\text{NLPF}} - k_1V_{\text{in}} \quad (7)$$

According to Equations (4), (6), and (7), the first proposed VM second-order multi-function filter system structure can be synthesized. The output signals of NLPF and NBPF, and the first filter parameters of ω_o and Q can be derived as follows.

$$\frac{V_{\text{NBPF}}}{V_{\text{in}}} = \frac{s\frac{k_1}{\tau_1}}{s^2 + s\frac{k_1}{\tau_1} + \frac{1}{\tau_1\tau_2}} \quad (8)$$

$$\frac{V_{\text{NLPF}}}{V_{\text{in}}} = \frac{k_1\frac{1}{\tau_1\tau_2}}{s^2 + s\frac{k_1}{\tau_1} + \frac{1}{\tau_1\tau_2}} \quad (9)$$

$$\omega_o = \sqrt{\frac{1}{\tau_1\tau_2}} \quad (10)$$

$$Q = \frac{1}{k_1} \sqrt{\frac{\tau_1}{\tau_2}} \quad (11)$$

Equations (10) and (11) indicate that the parameter Q can be independently tuned by adjusting the voltage gain building block of k_1 without affecting the parameter ω_o . In the special case of $\tau_1 = \tau_2 = \tau$, the parameter ω_o can also be independently tuned by τ without affecting the parameter Q . Based on the DC bias current I_B of the corresponding LT1228, the first proposed filter parameters of ω_o and Q can be controlled electronically and orthogonally.

In Equation (1), the VM IHPF second-order transfer function is decomposed into the VM NLPF and NBPF second-order transfer functions, and the synthesis of the system block diagram can be achieved. Equations (4), (6), and (7) can be rearranged as Equation (12) in the form of an input–output matrix, and the system block diagram synthesis for the first proposed VM LT1228-based filter design is shown in Figure 1. It uses one input voltage node and three output voltage nodes, and consists of a non-inverting lossless integrator, an inverting lossless integrator, and a voltage gain building block.

$$\begin{bmatrix} 1 & 0 & \frac{1}{s\tau_1} \\ -\frac{1}{s\tau_2} & 1 & 0 \\ -k_1 & -1 & 1 \end{bmatrix} \begin{bmatrix} V_{\text{NBPF}} \\ V_{\text{NLPF}} \\ V_{\text{IHPF}} \end{bmatrix} = \begin{bmatrix} 0 \\ 0 \\ -k_1V_{\text{in}} \end{bmatrix} \quad (12)$$

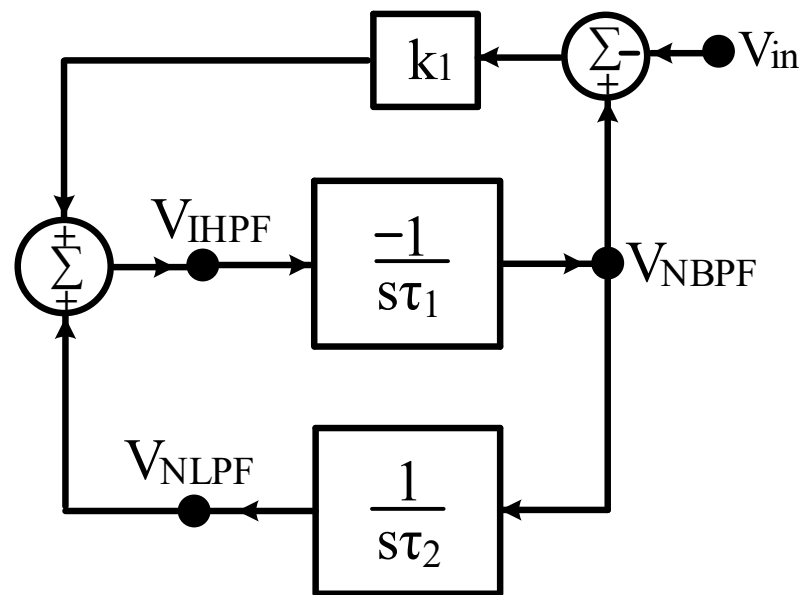


Figure 1. Synthesis of the first proposed VM LT1228-based filter system module with two integrator loops and a voltage gain building block.

In Figure 1, taking the system blocks of $\tau_1 = C_1/g_{m1}$, $\tau_2 = C_2/g_{m2}$ and $k_1 = g_{m3}R$, Equation (12) can be rewritten as

$$\begin{bmatrix} 1 & 0 & \frac{g_{m1}}{sC_1} \\ -\frac{g_{m2}}{sC_2} & 1 & 0 \\ -g_{m3}R & -1 & 1 \end{bmatrix} \begin{bmatrix} V_{NBPF} \\ V_{NLPF} \\ V_{IHPF} \end{bmatrix} = \begin{bmatrix} 0 \\ 0 \\ -g_{m3}RV_{in} \end{bmatrix} \quad (13)$$

where C_1 and C_2 are two capacitors, g_{m1} , g_{m2} , and g_{m3} are three LT1228 transconductance amplifiers, and R is a resistor. Solving Equation (13), the parameters ω_o and Q of the first filter and the three VM second-order transfer functions of the NBPF, NLPF and IHPF can be obtained as follows.

$$\frac{V_{NBPF}}{V_{in}} = \frac{sC_2g_{m1}g_{m3}R}{s^2C_1C_2 + sC_2g_{m1}g_{m3}R + g_{m1}g_{m2}} \quad (14)$$

$$\frac{V_{NLPF}}{V_{in}} = \frac{g_{m1}g_{m2}g_{m3}R}{s^2C_1C_2 + sC_2g_{m1}g_{m3}R + g_{m1}g_{m2}} \quad (15)$$

$$\frac{V_{IHPF}}{V_{in}} = \frac{-s^2C_1C_2g_{m3}R}{s^2C_1C_2 + sC_2g_{m1}g_{m3}R + g_{m1}g_{m2}} \quad (16)$$

$$\omega_o = \sqrt{\frac{g_{m1}g_{m2}}{C_1C_2}} \quad (17)$$

$$Q = \frac{1}{g_{m3}R} \sqrt{\frac{C_1g_{m2}}{C_2g_{m1}}} \quad (18)$$

Equations (17) and (18) indicate that the parameter Q can be independently tuned by adjusting g_{m3} and/or R without affecting the parameter ω_o . In the special case of $C_1 = C_2$, and $g_{m1} = g_{m2} = g_m$, the parameter ω_o can also be independently tuned by g_m without affecting the parameter Q . Based on the DC bias current I_B of the corresponding LT1228, the filter parameters of ω_o and Q can be controlled electronically and orthogonally. Based on Figure 1 and Equation (13), Section 2.2 discusses the first proposed high-input impedance electronically tunable VM one-input five-output second-order multifunction filter based on three LT1228 ICs.

2.2. First Proposed VM LT1228-Based Second-Order Multifunction Filter

The LT1228 contains a g_m transconductance amplifier with a DC bias current I_B and a wide range of voltage-gain [33,49]. Figure 2a,b show the circuit symbol for the commercial LT1228 IC and the package for the 8-pin IC configuration, respectively. In Figure 2b, the g_m transconductance differential voltages of V_+ and V_- have high-input impedance, the current output at Y terminal has high-output impedance, and the voltage at X terminal follows the voltage at Y terminal. The W terminal voltage has good linearity and can be directly connected to an external low resistance value. Therefore, the W terminal of the commercial LT1228 IC is suitable for driving low-impedance loads such as loudspeakers and cables. The supply voltages of V_{CC} and V_{EE} are the positive and negative supply voltages of the commercial LT1228 IC. The port factors of the LT1228 with high-input impedance V_+ and V_- , low-output impedance W and high-output impedance Y are important in the design of any analog circuits. Figure 3 shows the equivalent circuit of a commercial LT1228 IC, whose ideal property relations can be described by [32,33]:

$$\begin{bmatrix} I_{V+} \\ I_{V-} \\ I_y \\ V_x \\ V_w \end{bmatrix} = \begin{bmatrix} 0 & 0 & 0 & 0 & 0 \\ 0 & 0 & 0 & 0 & 0 \\ g_m & -g_m & 0 & 0 & 0 \\ 0 & 0 & 1 & 0 & 0 \\ 0 & 0 & 0 & R_T & 0 \end{bmatrix} \begin{bmatrix} V_+ \\ V_- \\ V_y \\ I_x \\ I_w \end{bmatrix} \quad (19)$$

where R_T is the transresistance gain of LT1228 and ideal value of R_T is close to infinity. The transconductance g_m of LT1228 depends on the I_B and the g_m -value can be described as [32,49]

$$g_m = 10I_B = \frac{V_{CC} - V_{EE} - 2V_{BE}}{R_B} \quad (20)$$

where R_B is the bias current control resistor.

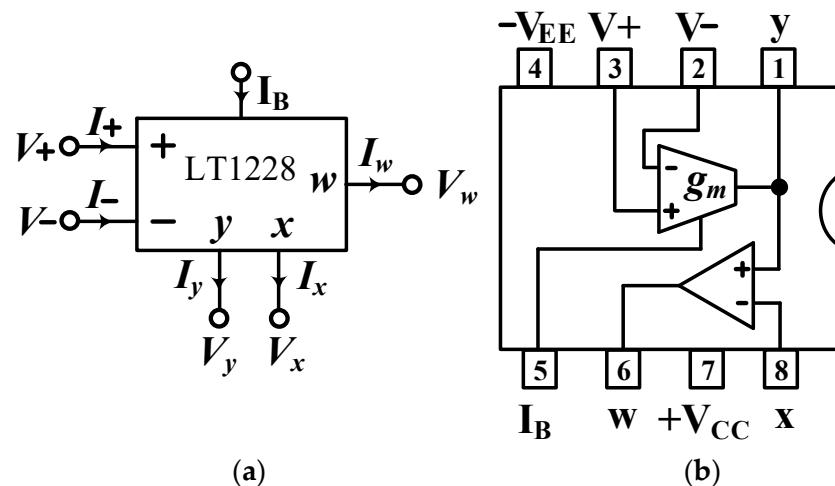


Figure 2. LT1228 (a) circuit symbol, and (b) IC package in an 8-pin configuration.

Based on the synthesis of the system block diagram in Figure 1, the first proposed VM LT1228-based second-order multifunction filter configuration using three commercial LT1228s, five resistors, and two capacitors connected to the ground is shown in Figure 4. The nodal analysis of the first proposed VM LT1228-based second-order multifunction filter configuration can be written as follows.

$$V_{o1} = -\frac{g_{m1}}{sC_1} V_{o3} \quad (21)$$

$$V_{o2} = \frac{g_{m2}}{sC_2} V_{o1} \quad (22)$$

$$V_{o3} = g_{m3}R(V_{o1} - V_{in}) + V_{o2} \quad (23)$$

$$V_{o4} = \left(1 + \frac{R_1}{R_2}\right)V_{o1} \quad (24)$$

$$V_{o5} = \left(1 + \frac{R_3}{R_4}\right)V_{o2} \quad (25)$$

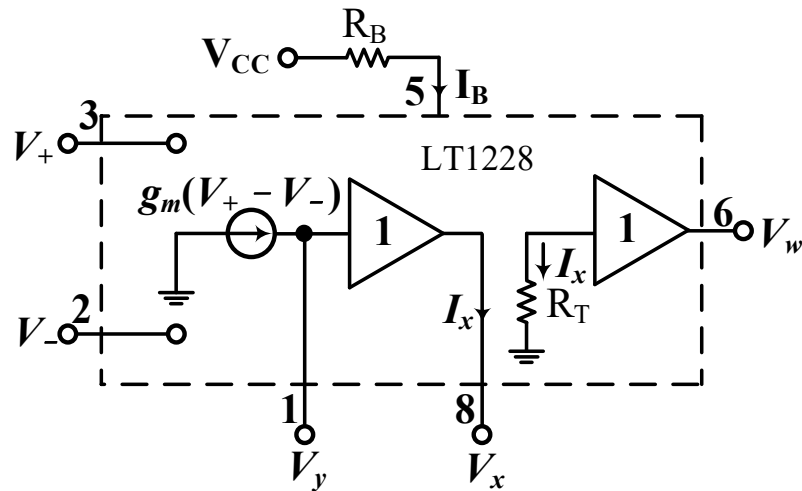


Figure 3. Equivalent circuit of LT1228.

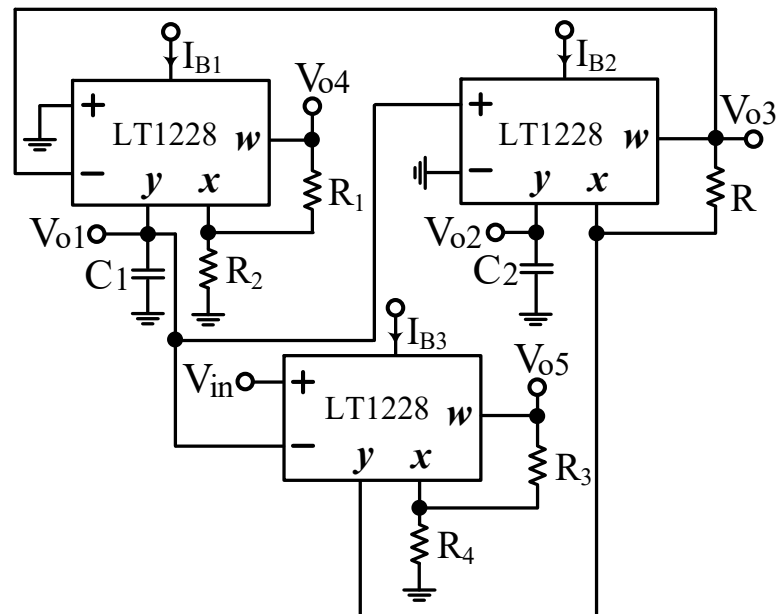


Figure 4. First proposed VM LT1228-based second-order multifunction filter configuration.

Equations (21)–(23) can be rearranged in the form of an input–output matrix equation as follows.

$$\begin{bmatrix} 1 & 0 & \frac{g_{m1}}{sC_1} \\ -\frac{g_{m2}}{sC_2} & 1 & 0 \\ -g_{m3}R & -1 & 1 \end{bmatrix} \begin{bmatrix} V_{o1} \\ V_{o2} \\ V_{o3} \end{bmatrix} = \begin{bmatrix} 0 \\ 0 \\ -g_{m3}RV_{in} \end{bmatrix} \quad (26)$$

Equation (26) is the same as Equation (13), if we let the outputs $V_{o1} = V_{NBPF}$, $V_{o2} = V_{NLPF}$, and $V_{o3} = V_{HPF}$. Therefore, the first proposed VM LT1228-based second-order multifunc-

tion filter proposed in Figure 4 simultaneously provides the NBPF, NLPF, and IHPF transfer functions at the V_{o1} , V_{o2} , and V_{o3} outputs, respectively, as shown in Equations (27)–(29).

$$\frac{V_{o1}}{V_{in}} = \frac{sC_2g_{m1}g_{m3}R}{s^2C_1C_2 + sC_2g_{m1}g_{m3}R + g_{m1}g_{m2}} \quad (27)$$

$$\frac{V_{o2}}{V_{in}} = \frac{g_{m1}g_{m2}g_{m3}R}{s^2C_1C_2 + sC_2g_{m1}g_{m3}R + g_{m1}g_{m2}} \quad (28)$$

$$\frac{V_{o3}}{V_{in}} = \frac{-s^2C_1C_2g_{m3}R}{s^2C_1C_2 + sC_2g_{m1}g_{m3}R + g_{m1}g_{m2}} \quad (29)$$

Based on Equations (27)–(29), the first proposed filter parameters of ω_o and Q are the same as Equations (17) and (18). According to Equations (24) and (25), the first proposed VM LT1228-based second-order multifunction filter has two independent gain-controlled BPF and LPF transfer functions at V_{o4} and V_{o5} output terminals, respectively, as shown in Equations (30) and (31).

$$\frac{V_{o4}}{V_{in}} = \left(1 + \frac{R_1}{R_2}\right) \frac{sC_2g_{m1}g_{m3}R}{s^2C_1C_2 + sC_2g_{m1}g_{m3}R + g_{m1}g_{m2}} \quad (30)$$

$$\frac{V_{o5}}{V_{in}} = \left(1 + \frac{R_3}{R_4}\right) \frac{g_{m1}g_{m2}g_{m3}R}{s^2C_1C_2 + sC_2g_{m1}g_{m3}R + g_{m1}g_{m2}} \quad (31)$$

In Equations (30) and (31), the first filter has two independent gain-controlled BPF and LPF transfer functions at the V_{o4} and V_{o5} outputs, and its four resistors of R_1 , R_2 , R_3 and R_4 can be tuned to independent gain control without affecting the design parameters of ω_o and Q . In Figure 4, the three output voltage nodes V_{o3} , V_{o4} , and V_{o5} are connected to the corresponding W terminal of each LT1228 to provide low output impedance. If $C_1 = C_2 = C$, $g_{m1} = g_{m2} = 10I_{B1}$ and $g_{m3} = 10I_{B3}$, the parameters ω_o and Q in Equations (17) and (18) can be rewritten as

$$\omega_o = \frac{10I_{B1}}{C} \quad (32)$$

$$Q = \frac{1}{10I_{B3}R} \quad (33)$$

In this particular case, the parameter ω_o can be tuned electronically and independently by the bias current I_{B1} of LT1228 without affecting the parameter Q , and the parameter Q can also be tuned electronically and independently by the bias current I_{B3} of LT1228 without affecting the parameter ω_o .

2.3. Second Proposed Synthesis Principle and Analysis Theory Based on Non-Inverting HPF Transfer Function

To synthesize the second proposed VM second-order multifunction filter design system block, the VM non-inverting HPF (NHPF) second-order transfer function with two integrator time constants τ_3 and τ_4 and a voltage passband gain k_2 can be considered as the following function.

$$\frac{V_{NHPF}}{V_{in}} = \frac{k_2s^2}{s^2 + s\frac{k_2}{\tau_3} + \frac{1}{\tau_3\tau_4}} \quad (34)$$

where V_{NHPF} is one of the output voltages of the second proposed filter, and V_{in} is the input voltage signal of the circuit

To decompose the VM NHPF second-order transfer function into the VM inverting LPF (ILPF) and NBPF transfer functions, the terms of Equation (34) can be cross-multiplied first, and then divided by s^2 to obtain

$$V_{NHPF} = -\frac{k_2}{s\tau_3}V_{NHPF} - \frac{1}{s^2\tau_3\tau_4}V_{NHPF} + k_2V_{in} \quad (35)$$

Rearranging Equation (35) can be rewritten as

$$V_{\text{NHPF}} = -\left(k_2 + \frac{1}{s\tau_4}\right)\left(\frac{1}{s\tau_3}V_{\text{NHPF}}\right) + k_2V_{\text{in}} \quad (36)$$

Let

$$V_{\text{NBPF}} = \frac{1}{s\tau_3}V_{\text{NHPF}} \quad (37)$$

This indicates that the NBPF signal can be achieved by cascading the NHPF signal with a non-inverting loss integrator, and Equation (37) becomes

$$V_{\text{NHPF}} = -k_2V_{\text{NBPF}} - \frac{1}{s\tau_4}V_{\text{NBPF}} + k_2V_{\text{in}} \quad (38)$$

Let

$$V_{\text{ILPF}} = -\frac{1}{s\tau_4}V_{\text{NBPF}} \quad (39)$$

This means that the ILPF signal can be achieved by cascading the NBPF signal with an inverting loss integrator, and Equation (39) becomes

$$V_{\text{NHPF}} = -k_2V_{\text{NBPF}} + V_{\text{ILPF}} + k_2V_{\text{in}} \quad (40)$$

According to Equations (37), (39), and (40), the second proposed VM second-order multifunction filter system structure can be synthesized. The output signals of NBPF and ILPF, and the second filter parameters of ω_o and Q can be derived as follows.

$$\frac{V_{\text{NBPF}}}{V_{\text{in}}} = \frac{s\frac{k_2}{\tau_3}}{s^2 + s\frac{k_2}{\tau_3} + \frac{1}{\tau_3\tau_4}} \quad (41)$$

$$\frac{V_{\text{ILPF}}}{V_{\text{in}}} = \frac{-k_2\frac{1}{\tau_3\tau_4}}{s^2 + s\frac{k_2}{\tau_3} + \frac{1}{\tau_3\tau_4}} \quad (42)$$

$$\omega_o = \sqrt{\frac{1}{\tau_3\tau_4}} \quad (43)$$

$$Q = \frac{1}{k_2} \sqrt{\frac{\tau_3}{\tau_4}} \quad (44)$$

Equations (43) and (44) indicate that the parameter Q can be independently tuned by adjusting the voltage gain building block of k_2 without affecting the parameter ω_o . In the special case of $\tau_3 = \tau_4 = \tau$, the parameter ω_o can also be independently tuned by τ without affecting the parameter Q . Based on the DC bias current I_B of the corresponding LT1228, the second proposed filter parameters of ω_o and Q can be controlled electronically and orthogonally.

In Equation (34), the VM NHPF second-order transfer function is decomposed into the VM NBPF and ILPF second-order transfer functions, and the synthesis of the system block diagram can be achieved. Equations (37), (39), and (40) can be rearranged as Equation (45) in the form of an input–output matrix equation, and the system block diagram synthesis for the second proposed VM LT1228-based second-order multifunction filter design is shown in Figure 5. It uses one input voltage node and three output voltage nodes, and consists of a non-inverting lossless integrator, an inverting lossless integrator, and a voltage gain building block.

$$\begin{bmatrix} 1 & 0 & -\frac{1}{s\tau_3} \\ \frac{1}{s\tau_4} & 1 & 0 \\ k_2 & -1 & 1 \end{bmatrix} \begin{bmatrix} V_{\text{NBPF}} \\ V_{\text{ILPF}} \\ V_{\text{NHPF}} \end{bmatrix} = \begin{bmatrix} 0 \\ 0 \\ k_2V_{\text{in}} \end{bmatrix} \quad (45)$$

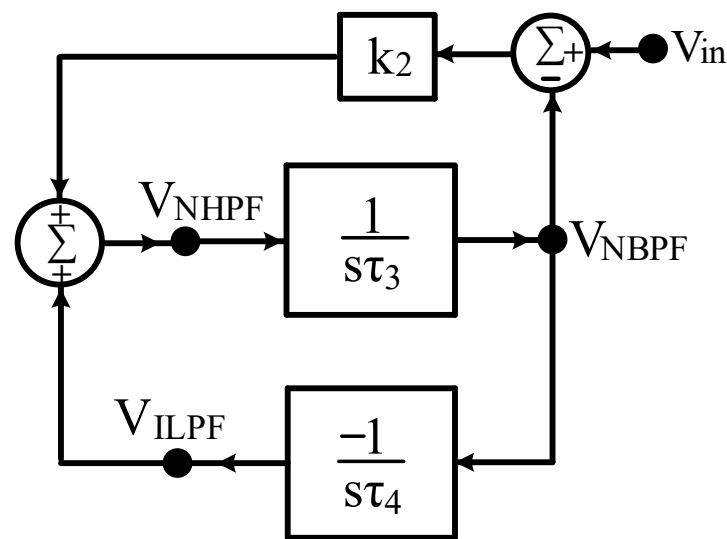


Figure 5. Synthesis of the second proposed VM LT1228-based filter system module with two integrator loops and a voltage gain building block.

In Figure 5, taking the system blocks of $\tau_3 = C_3/g_{m4}$, $\tau_4 = C_4/g_{m5}$, and $k_2 = g_{m6}R$, Equation (45) can be rewritten as

$$\begin{bmatrix} 1 & 0 & -\frac{g_{m4}}{sC_3} \\ \frac{g_{m5}}{sC_4} & 1 & 0 \\ g_{m6}R & -1 & 1 \end{bmatrix} \begin{bmatrix} V_{NBPF} \\ V_{ILPF} \\ V_{NHPF} \end{bmatrix} = \begin{bmatrix} 0 \\ 0 \\ g_{m6}RV_{in} \end{bmatrix} \quad (46)$$

where C_3 and C_4 are two capacitors, g_{m4} , g_{m5} , and g_{m6} are three LT1228 transconductance amplifiers, and R is a resistor. Solving Equation (46), the parameters ω_0 and Q of the second filter and the three VM second-order transfer functions of the NBPF, ILPF, and NHPF can be obtained as follows.

$$\frac{V_{NBPF}}{V_{in}} = \frac{sC_4g_{m4}g_{m6}R}{s^2C_3C_4 + sC_4g_{m4}g_{m6}R + g_{m4}g_{m5}} \quad (47)$$

$$\frac{V_{ILPF}}{V_{in}} = \frac{-g_{m4}g_{m5}g_{m6}R}{s^2C_3C_4 + sC_4g_{m4}g_{m6}R + g_{m4}g_{m5}} \quad (48)$$

$$\frac{V_{NHPF}}{V_{in}} = \frac{s^2C_3C_4g_{m6}R}{s^2C_3C_4 + sC_4g_{m4}g_{m6}R + g_{m4}g_{m5}} \quad (49)$$

$$\omega_0 = \sqrt{\frac{g_{m4}g_{m5}}{C_3C_4}} \quad (50)$$

$$Q = \frac{1}{g_{m6}R} \sqrt{\frac{C_3g_{m5}}{C_4g_{m4}}} \quad (51)$$

Equations (50) and (51) indicate that the parameter Q can be independently tuned by adjusting g_{m6} and/or R without affecting the parameter ω_0 . In the special case of $C_3 = C_4$, and $g_{m4} = g_{m5} = g_m$, the parameter ω_0 can also be independently tuned by g_m without affecting the parameter Q . Based on the DC bias current I_B of the corresponding LT1228, the filter parameters of ω_0 and Q can be controlled electronically and orthogonally. Based on Figure 5 and Equation (46), Section 2.4 discusses the second proposed high-input impedance electronically tunable VM one-input five-output second-order multifunction filter based on three LT1228 ICs.

2.4. Second Proposed VM LT1228-Based Second-Order Multifunction Filter

Based on the synthesis of the system block diagram in Figure 5, the second proposed VM LT1228-based second-order multifunction filter configuration using three commercial LT1228s, five resistors and two capacitors connected to the ground is shown in Figure 6. The nodal analysis of the second proposed VM LT1228-based second-order multifunction filter configuration can be written as follows.

$$V_{o1} = \frac{g_{m4}}{sC_3} V_{o3} \quad (52)$$

$$V_{o2} = -\frac{g_{m5}}{sC_4} V_{o1} \quad (53)$$

$$V_{o3} = g_{m3}R(V_{in} - V_{o1}) + V_{o2} \quad (54)$$

$$V_{o4} = \left(1 + \frac{R_5}{R_6}\right)V_{o1} \quad (55)$$

$$V_{o5} = \left(1 + \frac{R_7}{R_8}\right)V_{o2} \quad (56)$$

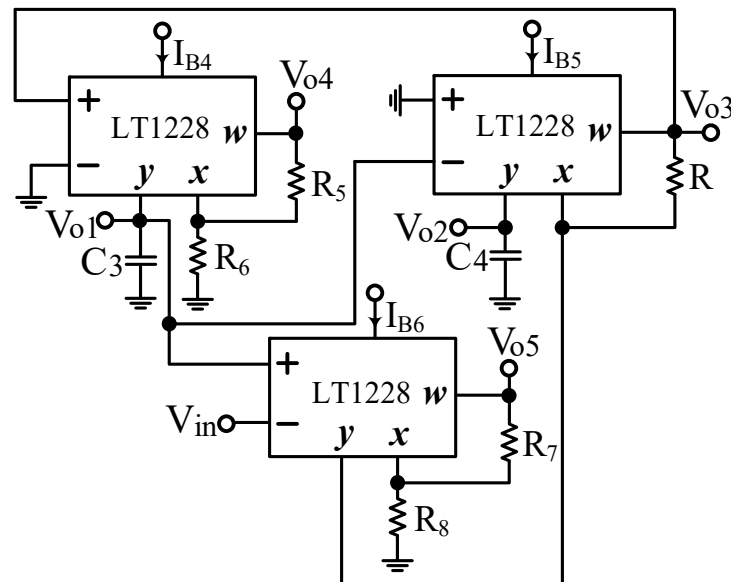


Figure 6. Second proposed VM LT1228-based second-order multifunction filter configuration.

Equations (52)–(54) can be rearranged in the form of an input–output matrix equation as follows.

$$\begin{bmatrix} 1 & 0 & -\frac{g_{m4}}{sC_3} \\ \frac{g_{m5}}{sC_4} & 1 & 0 \\ g_{m6}R & -1 & 1 \end{bmatrix} \begin{bmatrix} V_{o1} \\ V_{o2} \\ V_{o3} \end{bmatrix} = \begin{bmatrix} 0 \\ 0 \\ g_{m6}RV_{in} \end{bmatrix} \quad (57)$$

Equation (57) is the same as Equation (46), if we let the outputs $V_{o1} = V_{NBPF}$, $V_{o2} = V_{ILPF}$, and $V_{o3} = V_{NHPF}$. Therefore, the second proposed VM LT1228-based second-order multifunction filter proposed in Figure 6 simultaneously provides the NBPF, ILPF, and NHPF transfer functions at the V_{o1} , V_{o2} , and V_{o3} outputs, respectively, as shown in Equations (58)–(60).

$$\frac{V_{o1}}{V_{in}} = \frac{sC_4g_{m4}g_{m6}R}{s^2C_3C_4 + sC_4g_{m4}g_{m6}R + g_{m4}g_{m5}} \quad (58)$$

$$\frac{V_{o2}}{V_{in}} = \frac{-g_{m4}g_{m5}g_{m6}R}{s^2C_3C_4 + sC_4g_{m4}g_{m6}R + g_{m4}g_{m5}} \quad (59)$$

$$\frac{V_{o3}}{V_{in}} = \frac{s^2 C_3 C_4 g_{m6} R}{s^2 C_3 C_4 + s C_4 g_{m4} g_{m6} R + g_{m4} g_{m5}} \quad (60)$$

Based on Equations (58)–(60), the second proposed filter parameters of ω_o and Q are the same as Equations (50) and (51). According to Equations (55) and (56), the second proposed VM LT1228-based second-order multifunction filter has two independent gain-controlled BPF and LPF transfer functions at V_{o4} and V_{o5} output terminals, respectively, as shown in Equations (61) and (62).

$$\frac{V_{o4}}{V_{in}} = \left(1 + \frac{R_5}{R_6}\right) \left(\frac{s C_4 g_{m4} g_{m6} R}{s^2 C_3 C_4 + s C_4 g_{m4} g_{m6} R + g_{m4} g_{m5}}\right) \quad (61)$$

$$\frac{V_{o5}}{V_{in}} = \left(1 + \frac{R_7}{R_8}\right) \left(\frac{-g_{m4} g_{m5} g_{m6} R}{s^2 C_3 C_4 + s C_4 g_{m4} g_{m6} R + g_{m4} g_{m5}}\right) \quad (62)$$

In Equations (61) and (62), the second filter has two independent gain-controlled BPF and LPF transfer functions at the V_{o4} and V_{o5} outputs, and its four resistors of R_5 , R_6 , R_7 , and R_8 can be tuned to independent gain control without affecting the design parameters of ω_o and Q . In Figure 6, the three output voltage nodes V_{o3} , V_{o4} , and V_{o5} are connected to the corresponding W terminal of each LT1228 to provide low output impedance. If $C = C_3 = C_4$, $g_{m4} = g_{m5} = 10I_{B4}$, and $g_{m6} = 10I_{B6}$, the parameters ω_o and Q in Equations (50) and (51) can be rewritten as

$$\omega_o = \frac{10I_{B4}}{C} \quad (63)$$

$$Q = \frac{1}{10I_{B6}R} \quad (64)$$

In this particular case, the parameter ω_o can be tuned electronically and independently by the bias current I_{B4} of LT1228 without affecting the parameter Q , and the parameter Q can also be tuned electronically and independently by the bias current I_{B6} of LT1228 without affecting the parameter ω_o .

3. Simulation and Experimental Results

To verify the operation of the two proposed filter topologies in Figures 4 and 6, OrCAD PSpice simulations and experimental verifications were performed based on three commercially available LT1228 ICs. Figures 7 and 8 show the top and bottom views of the printed circuit board (PCB) hardware implementation of the two proposed VM LT1228-based second-order multifunction filters in Figures 4 and 6, respectively. The supply voltage for each circuit is ± 15 V. Each power dissipation (PD) calculated in Figures 7 and 8 using the Keithley 2231A-30-3 power supply is 0.69 W. Figures 9 and 10 illustrate the experimental hardware setup used to verify the filter topologies designed in Figures 4 and 6, respectively.

3.1. Verification of the First Proposed VM LT1228-Based Multifunction Filter

To verify the operability of the first proposed VM LT1228-based multifunction filter at $f_o = 159.15$ kHz and $Q = 1$, two capacitors $C_1 = C_2 = 1$ nF, five resistors $R = R_1 = R_2 = R_3 = R_4 = 1$ k Ω , and three commercial LT1228 ICs with bias currents of $I_{B1} = I_{B2} = I_{B3} = 100$ μ A were chosen. Figures 11–15 illustrate the simulation results of the filter magnitude and phase responses of the first proposed circuit in Figure 4. From Figures 11–15, the first proposed VM LT1228-based multifunction filter provides five output responses in the frequency-domain. Figure 16 shows that the simulation results of the Q -value can specify the recommended independent control without affecting the pole frequency. In Figure 16, the simulated Q -value was varied for $Q = \{2.56, 4.06, 5.01, 5.95\}$ via the three bias currents $I_{B1} = I_{B2} = 100$ μ A and $I_{B3} = \{40, 25, 20, 16.6\}$ μ A. This is expected since the output swing distortion limits the Q -value below 6, and the Q -value error remains below 2%. Figure 17 shows the frequency tunability results of the first proposed filter simulated at the V_{o1} output voltage. In Figure 17, the simulated pole frequency was varied for $f_o = \{46.77, 125.02, 235.5, 961.61\}$ kHz via the

three bias currents $I_{B1} = I_{B2} = \{30, 80, 150, 600\}$ μA and $I_{B3} = 100$ μA . Figures 16 and 17 confirm that the first VM multifunction filter provides electronic control of the f_o and Q parameters. Figures 18 and 19 show the frequency tunability results of the first proposed filter simulated at the V_{o2} and V_{o3} output voltages, respectively. In Figure 18, the simulated pole frequency was varied for $f_o = \{46.61, 124.25, 387.61, 927.25\}$ kHz via the three bias currents $I_{B1} = I_{B2} = \{30, 80, 250, 600\}$ μA and $I_{B3} = 100$ μA . In Figure 19, the simulated pole frequency was varied for $f_o = \{46.63, 124.39, 389.22, 936.26\}$ kHz via the three bias currents $I_{B1} = I_{B2} = \{30, 80, 250, 600\}$ μA and $I_{B3} = 100$ μA . To demonstrate the stability of the first proposed multifunction filter at different temperatures, the NBPf (V_{o1}), NLPF (V_{o2}), and IHPF (V_{o3}) of the first circuit are operated at different temperatures. Figures 20–22 show the NBPf, NLPF, and IHPF operating at different temperatures, respectively. From Figures 20–22 it can be seen that the temperature varies from -5° to 50° . The simulated NBPf varies from 174.18 kHz to 144.54 kHz, which affects the operating pole frequency of 159.15 kHz in the range of 9.44% to -9.17% . The simulated NLPF varies from 173.78 kHz to 144.21 kHz, which affects the operating pole frequency of 159.15 kHz in the range 9.19% to -9.38% . The simulated IHPF varies from 174.18 kHz to 144.54 kHz, which affects the operating pole frequency of 159.15 kHz in the range 9.44% to -9.17% . Figures 23–27 illustrate the time-domain characteristics of the first proposed circuit when the frequency and amplitude of the input sine wave are 159.15 kHz and 180 m V_{pp} , respectively. Table 2 shows the measured phase error between the output and input waveforms at an operating pole frequency of 159.15 kHz. In Table 2, the maximum phase error measured in the time-domain at an operating pole frequency of 159.15 kHz is less than 0.97° . Figure 28 shows the NBPf total harmonic distortion (THD) measured at V_{o1} versus different input voltage signals. In Figure 28, the THD is below 2% when the input peak-to-peak voltage increases to 220 m V_{pp} . Figure 29 illustrates the simulated noise performance at the V_{o1} output voltage of the first proposed circuit. As shown in Figure 29, the total equivalent input and output noise voltages at the operating pole frequency were 86.33 and 86.44 nV/ $\sqrt{\text{Hz}}$, respectively. Figures 30–34 show the first filter magnitude and phase responses measured by the Keysight E5061B-3L5 network analyzer for the first proposed circuit in Figure 4. Figures 35–39 illustrate the calculated, simulated, and measured filter amplitude and phase responses for the first proposed circuit in Figure 4. Based on the ideal pole phase marked in the frequency-domain characteristics, Table 3 shows the simulated and measured pole frequency errors for the first proposed circuit. In Table 3, the maximum percentage error of the pole frequency measured in the frequency-domain is less than 1.22%. According to Figures 35–39 and Table 3, the amplitude and phase responses of the first proposed circuit agree with the simulated and measured results.

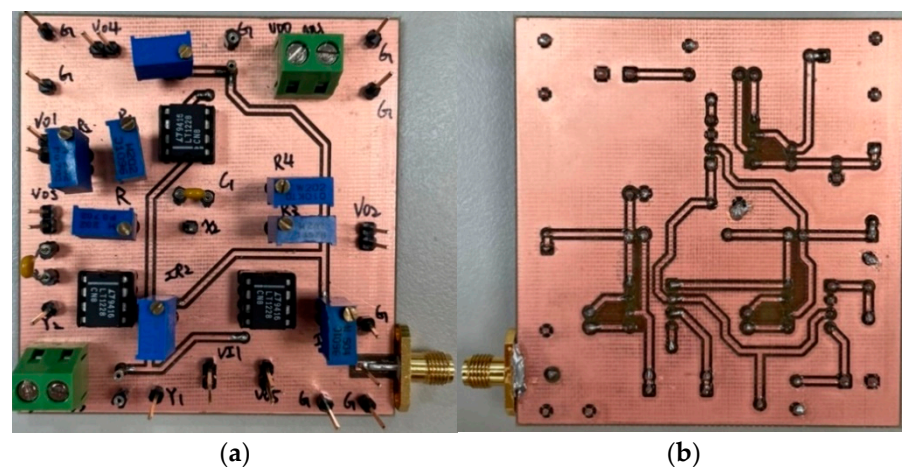


Figure 7. (a) Top and (b) bottom photos of the first proposed VM LT1228-based multifunction filter PCB hardware implementation in Figure 4.

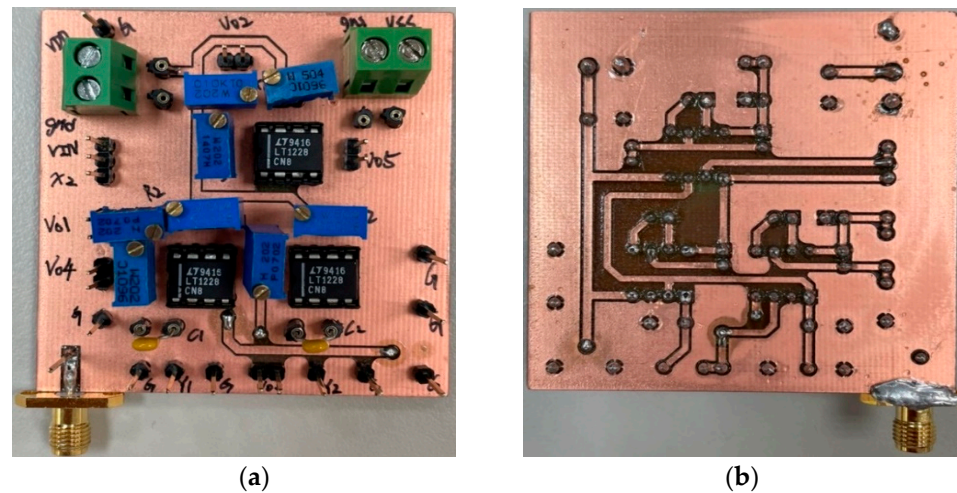


Figure 8. (a) Top and (b) bottom photos of the second proposed VM LT1228-based multifunction filter PCB hardware implementation in Figure 6.

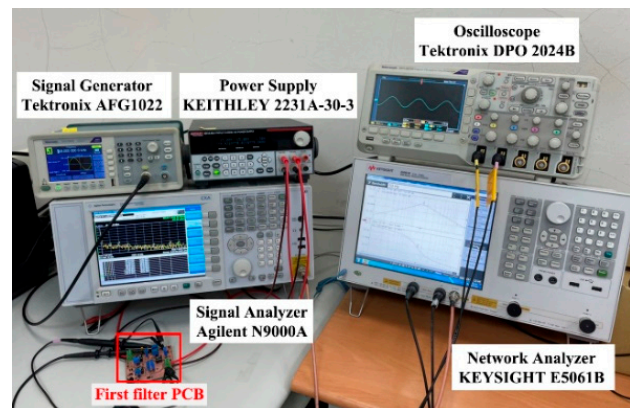


Figure 9. Experimental hardware setup of the first proposed VM LT1228-based multifunction filter in Figure 4.

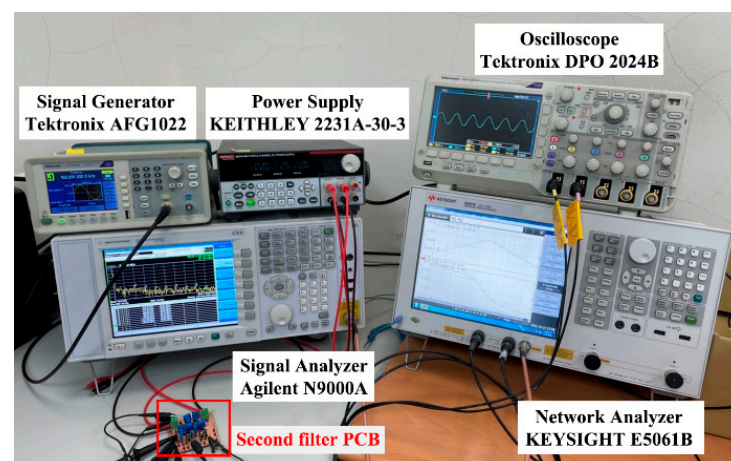


Figure 10. Experimental hardware setup of the second proposed VM LT1228-based multifunction filter in Figure 6.

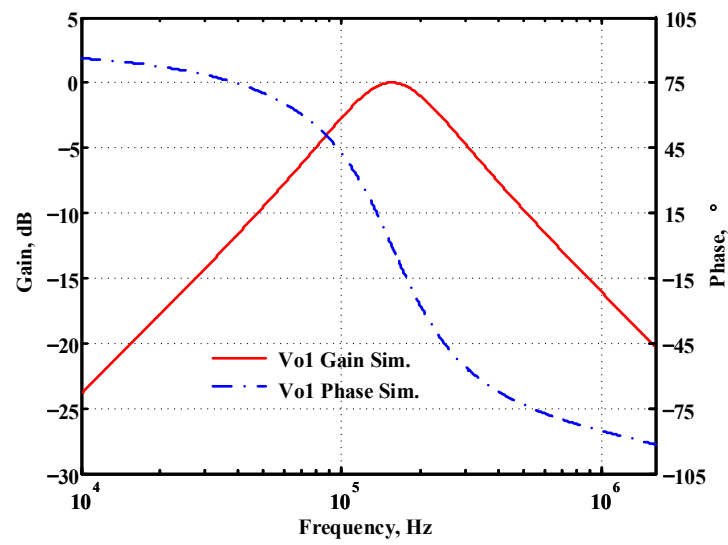


Figure 11. Simulated gain and phase frequency response of the first proposed circuit at V_{o1} .

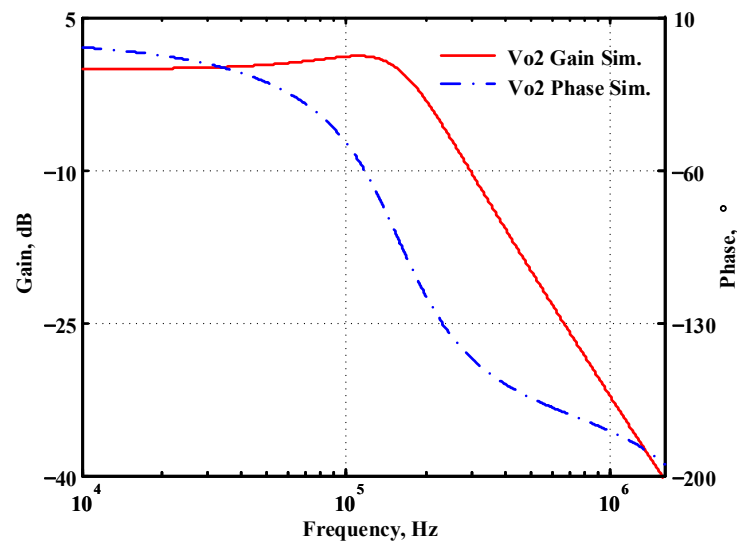


Figure 12. Simulated gain and phase frequency response of the first proposed circuit at V_{o2} .

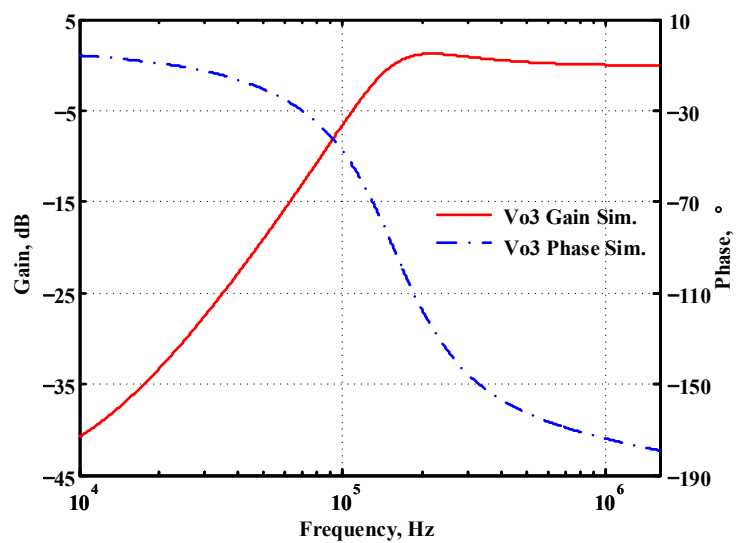


Figure 13. Simulated gain and phase frequency response of the first proposed circuit at V_{o3} .

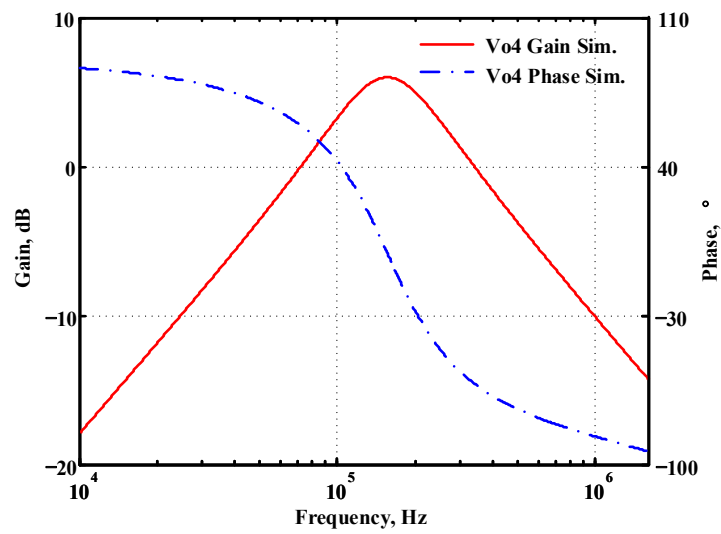


Figure 14. Simulated gain and phase frequency response of the first proposed circuit at V_{o4} .

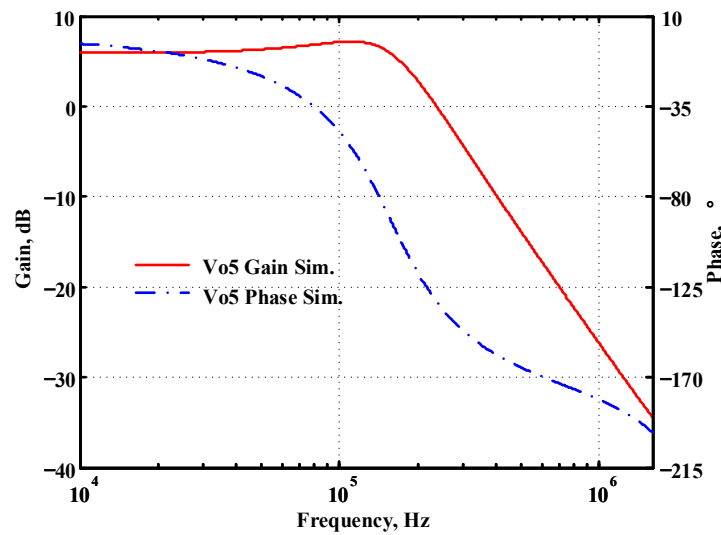


Figure 15. Simulated gain and phase frequency response of the first proposed circuit at V_{o5} .

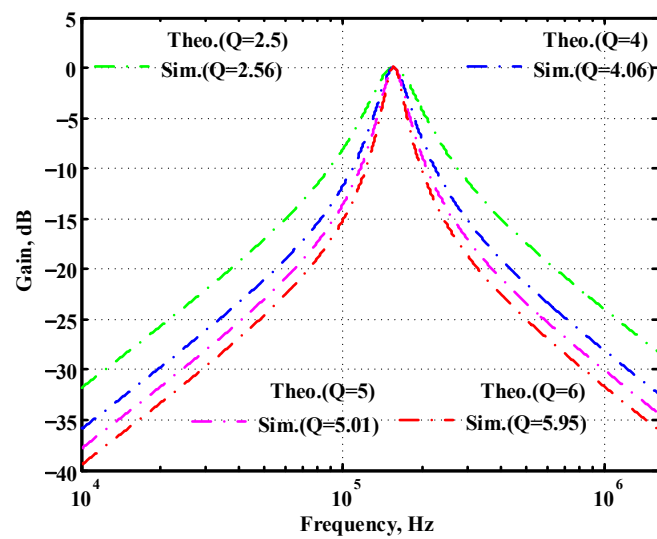


Figure 16. Simulated gain response of the first proposed circuit at V_{o1} by changing Q and keeping f_o constant.

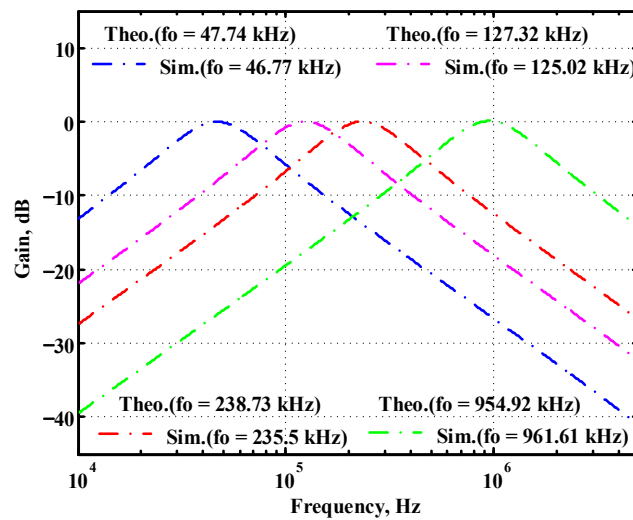


Figure 17. Simulated gain response of the first proposed circuit at V_{o1} by changing f_0 and keeping Q constant.

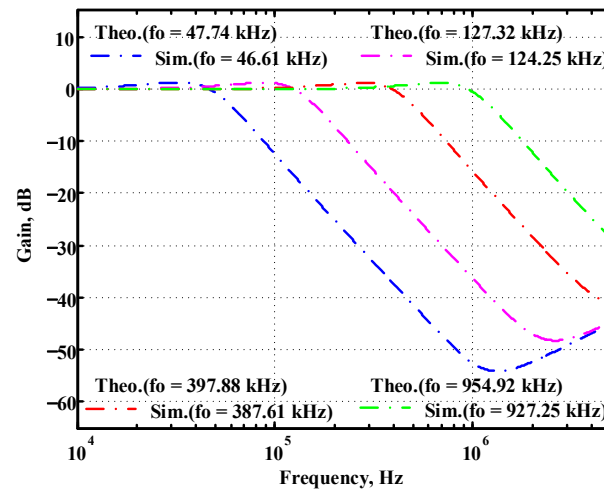


Figure 18. Simulated gain response of the first proposed circuit at V_{o2} by changing f_0 and keeping Q constant.

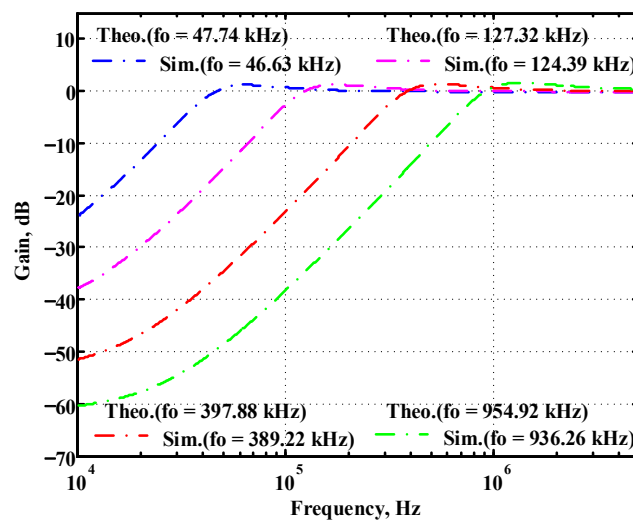


Figure 19. Simulated gain response of the first proposed circuit at V_{o3} by changing f_0 and keeping Q constant.

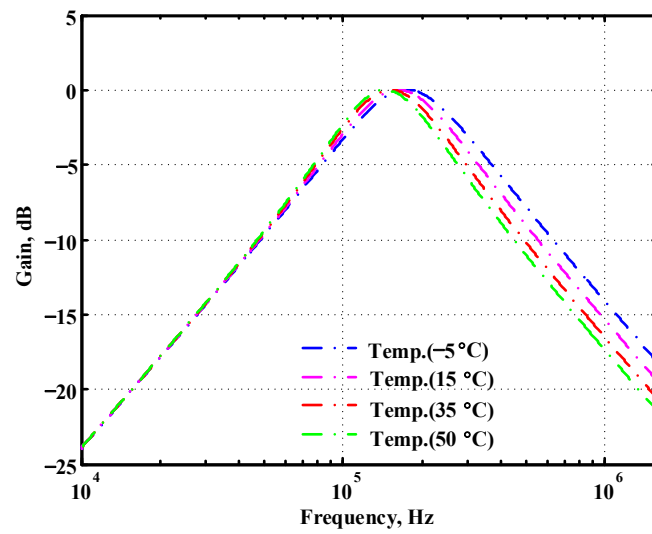


Figure 20. Simulated temperature variation at V_{o1} for the first proposed circuit.

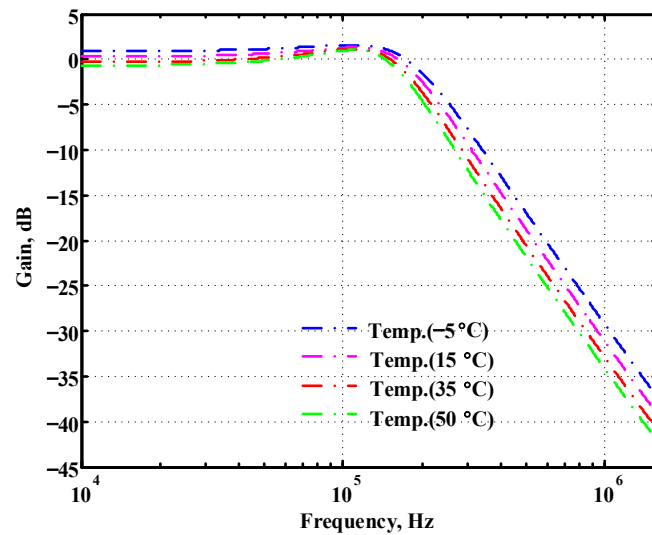


Figure 21. Simulated temperature variation at V_{o2} for the first proposed circuit.

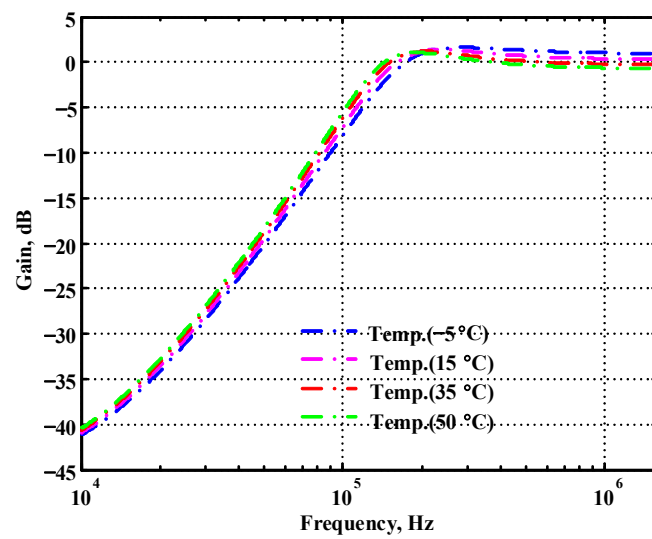


Figure 22. Simulated temperature variation at V_{o3} for the first proposed circuit.

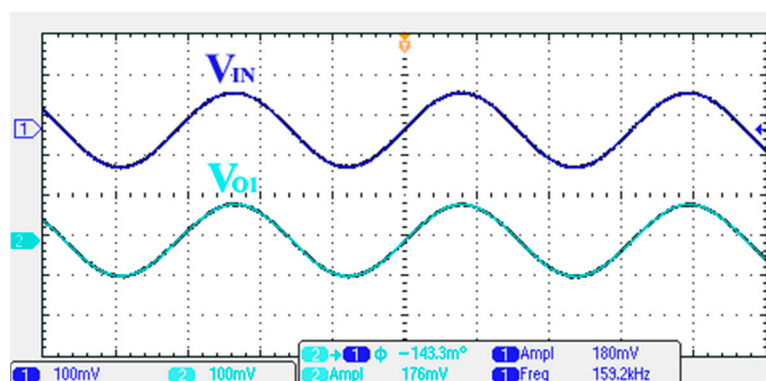


Figure 23. Measured output and input characteristics of the first proposed circuit at V_{O1} .

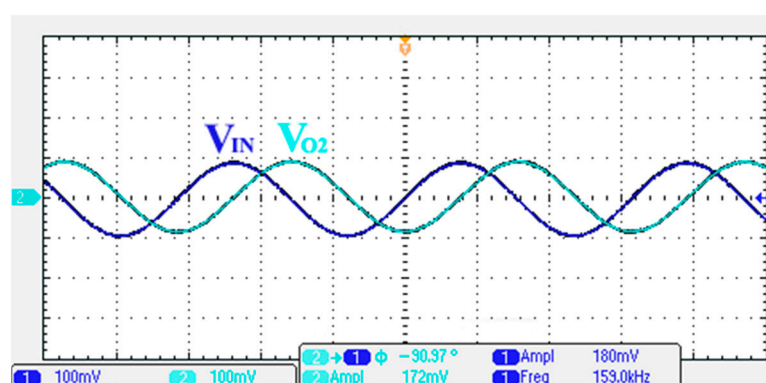


Figure 24. Measured output and input characteristics of the first proposed circuit at V_{O2} .

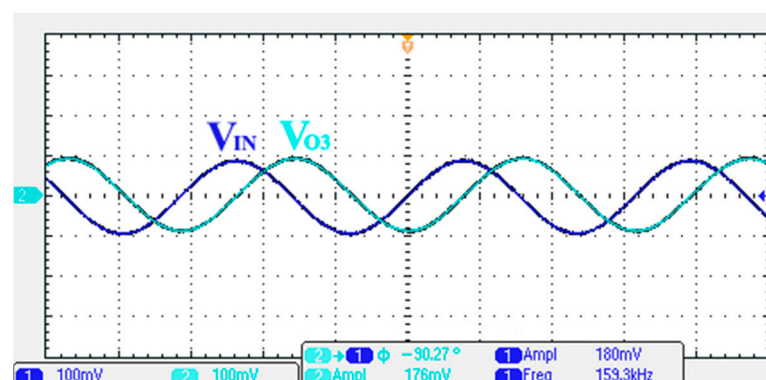


Figure 25. Measured output and input characteristics of the first proposed circuit at V_{O3} .

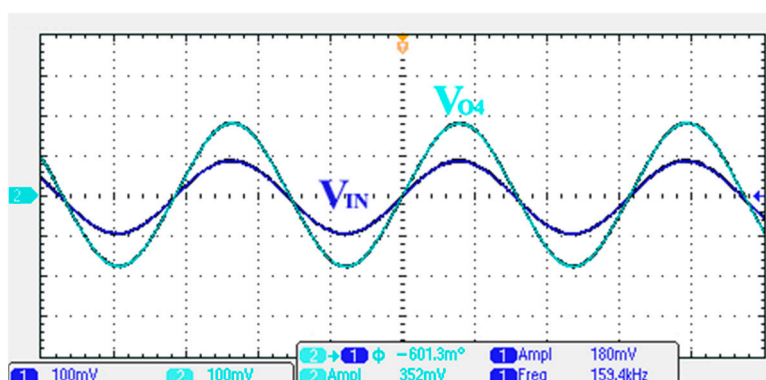


Figure 26. Measured output and input characteristics of the first proposed circuit at V_{O4} .

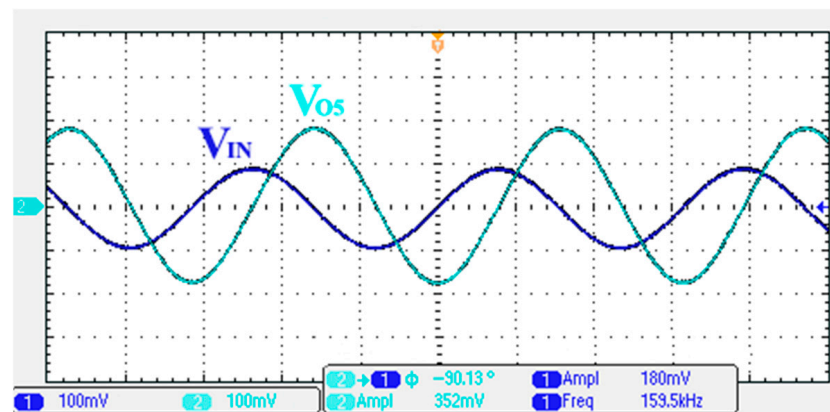


Figure 27. Measured output and input characteristics of the first proposed circuit at V_{o5} .

Table 2. Time domain characteristics of the output phase errors of the first proposed filter measured at 159.15 kHz.

Output Terminal	Operating Pole Phase		Output Phase Error
	Theoretical	Measured	
V_{o1}	0°	-0.143°	-0.143°
V_{o2}	-90°	-90.97°	-0.97°
V_{o3}	-90°	-90.27°	-0.27°
V_{o4}	0°	-0.601°	-0.601°
V_{o5}	-90°	-90.13°	-0.13°

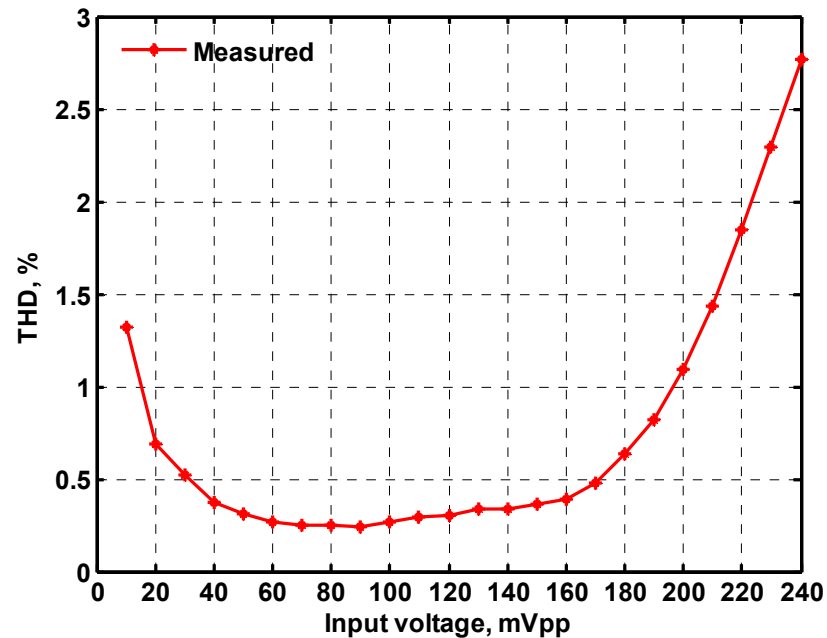


Figure 28. Measured THD of the first proposed circuit at V_{o1} in Figure 4 versus peak-to-peak input voltage signal at 159.15 kHz.

In both simulations and measurements, the bias current I_B of commercial LT1228 IC was tuned in the range of 30 to 600 μA , making the first filter's pole frequency f_o easily adjustable in the range of 47.74 to 954.92 kHz. Figures 40 and 41 show the frequency tunability results of the first proposed filter measured at the V_{o1} output voltage. In Figure 40, the measured pole frequency varied for $f_o = \{94.92, 189.21, 349.03, 635.39\}$ kHz via the three bias currents $I_{B1} = I_{B2} = \{60, 120, 220, 400\}$ μA and $I_{B3} = 100$ μA . In Figure 41, the

measured pole frequency varied for $f_o = \{47.2, 126.56, 236.18, 951.94\}$ kHz via the three bias currents $I_{B1} = I_{B2} = \{30, 80, 150, 600\}$ μA and $I_{B3} = 100$ μA . Figures 42 and 43 illustrate the calculated, simulated, and measured filter amplitude responses at the V_{o1} output voltage. As shown in Figures 42 and 43, the electronic tunability of the first filter parameter f_o does not affect the parameter Q . Figure 44 shows the quality factor tunability results for the first proposed filter at the V_{o1} output voltage. In Figure 44, the measured quality factor varied for $Q = \{0.92, 1.56, 1.97, 2.79\}$ via the three bias currents $I_{B1} = I_{B2} = 100$ μA and $I_{B3} = \{142, 66.6, 50, 33.3\}$ μA . Figure 45 illustrates the calculated, simulated, and measured amplitude responses of the first filter at the V_{o1} output voltage. As shown in Figure 45, the electronic tunability of the first filter parameter Q does not affect the parameter f_o . To show the linearity of the first proposed VM LT1228-based multifunction filter in Figure 4, a 1-dB power gain compression point (P1dB) of the NBPf was measured at the V_{o1} output voltage. Figure 46 shows that the measured input P1dB point is approximately -7.1 dBm. Figure 47 shows the spectrum analysis measured at the V_{o1} output voltage of the first proposed circuit when the frequency and amplitude of the input sine wave are 159.15 kHz and 180 mV_{pp}, respectively. As shown in Figure 47, the spurious-free dynamic range (SFDR) between the first tone and the highest spur of the other levels is 45.02 dBc. To show the non-linearity of the first proposed circuit in Figure 4, a two-tone test has been performed. The intermodulation distortion (IMD) performance of the first proposed circuit at the V_{o1} output voltage is further investigated using equal-amplitude two-tone signals with frequencies $f_1 = 158.15$ kHz and $f_2 = 160.15$ kHz. Using the Keysight-Agilent N9000A CXA signal analyzer, Figure 48 illustrates the IMD results measured at the V_{o1} output voltage of the first proposed circuit. In Figure 48, the third-order IMD (IMD3) and third-order intercept (TOI) point were measured as -48.84 dBc and 4.133 dBm, respectively. Table 4 summarizes the measured performance of the first proposed VM LT1228-based second-order multifunction filter.

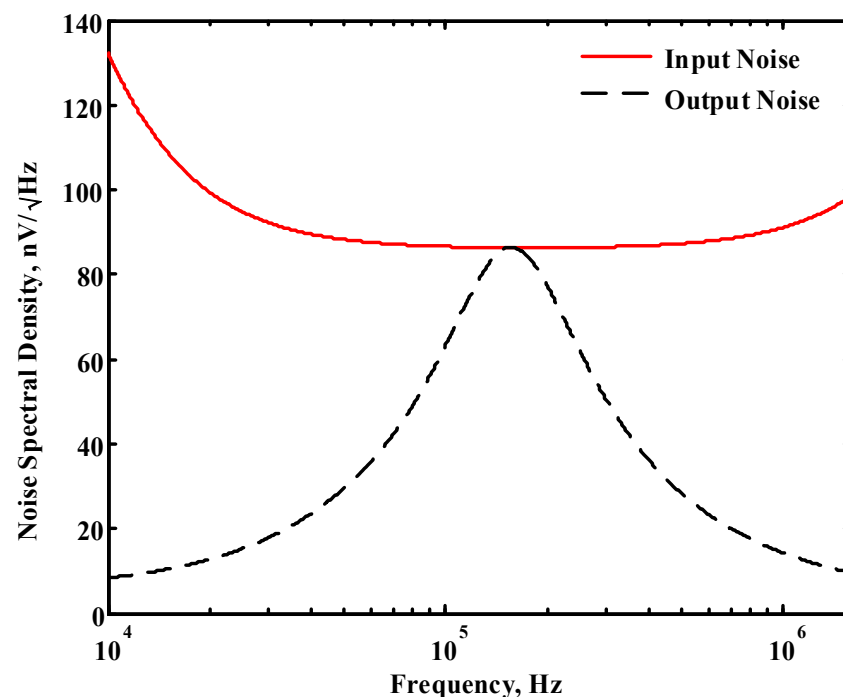


Figure 29. Simulated noise performance of the first proposed circuit at V_{o1} .



Figure 30. Frequency-domain characteristics of the measured amplitude and phase responses of the first proposed circuit at V_{O1} .



Figure 31. Frequency-domain characteristics of the measured amplitude and phase responses of the first proposed circuit at V_{O2} .

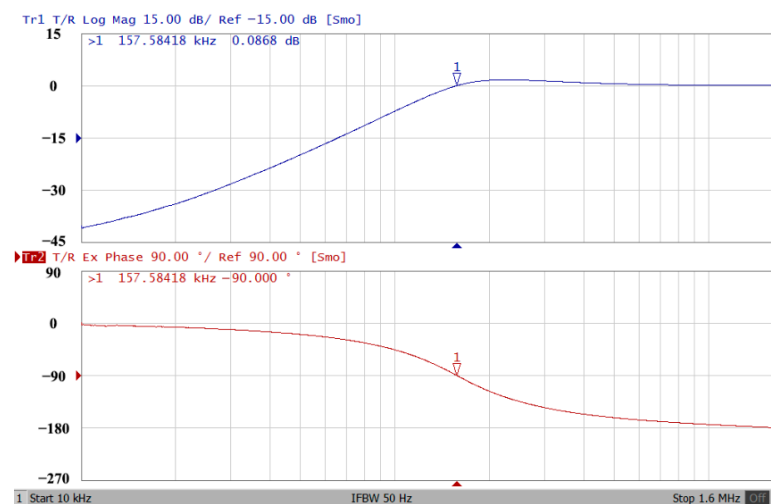


Figure 32. Frequency-domain characteristics of the measured amplitude and phase responses of the first proposed circuit at V_{O3} .

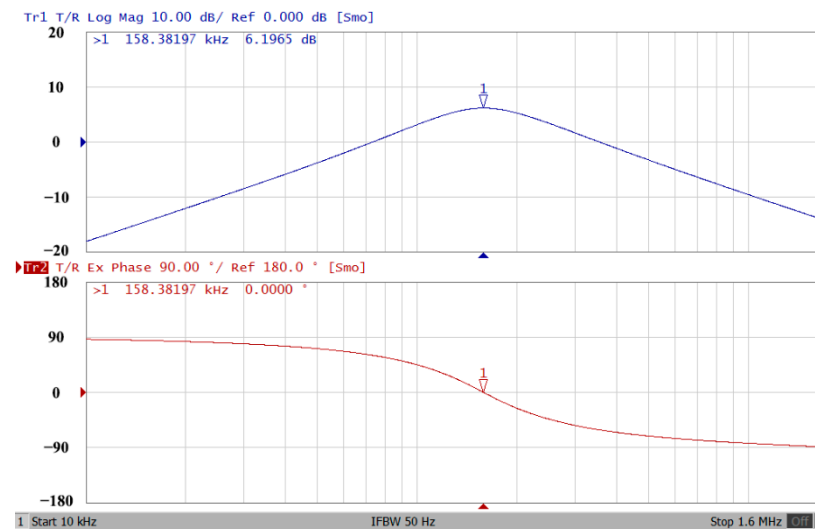


Figure 33. Frequency-domain characteristics of the measured amplitude and phase responses of the first proposed circuit at V_{04} .

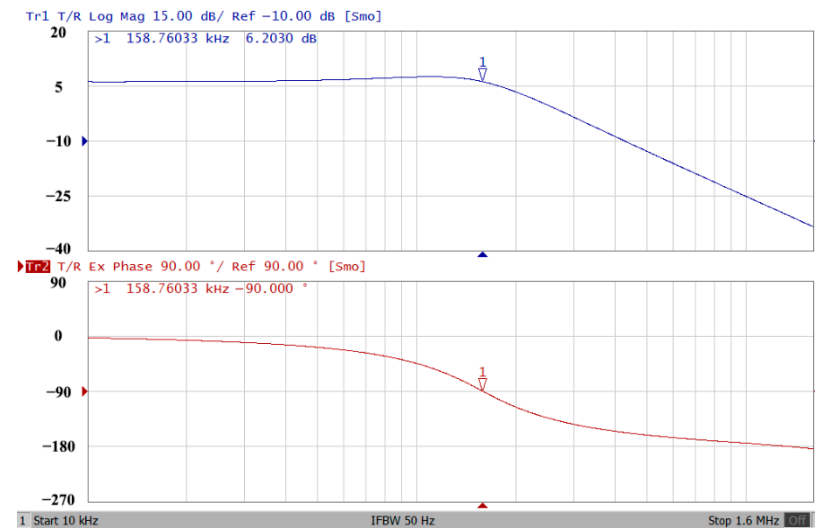


Figure 34. Frequency-domain characteristics of the measured amplitude and phase responses of the first proposed circuit at V_{05} .

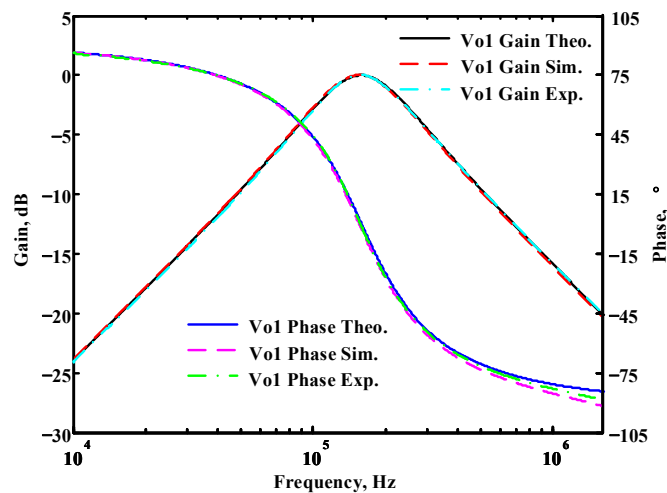


Figure 35. Simulated, measured, and theoretical comparison results of the first proposed circuit at V_{01} .

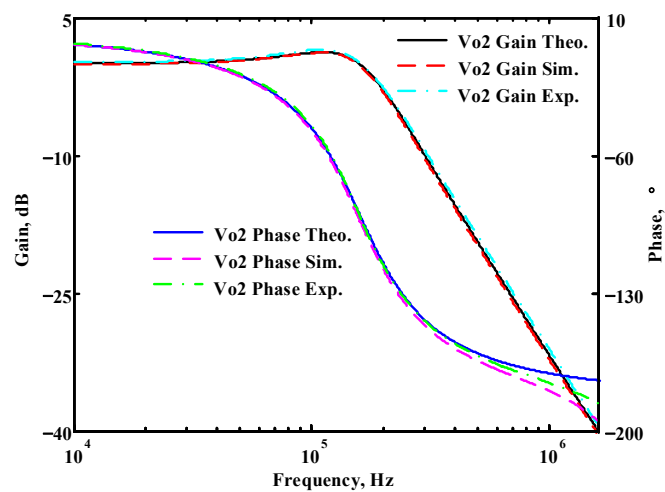


Figure 36. Simulated, measured, and theoretical comparison results of the first proposed circuit at V_{O2} .

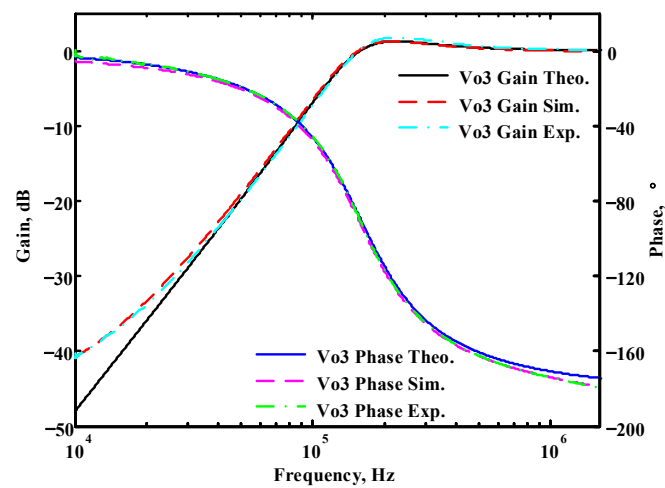


Figure 37. Simulated, measured, and theoretical comparison results of the first proposed circuit at V_{O3} .

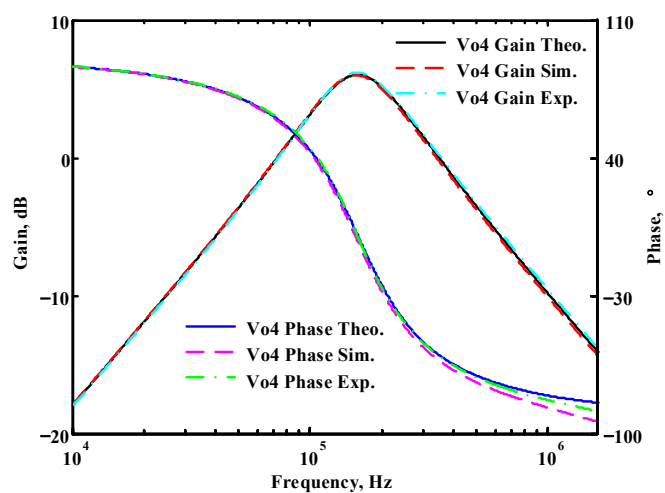


Figure 38. Simulated, measured, and theoretical comparison results of the first proposed circuit at V_{O4} .

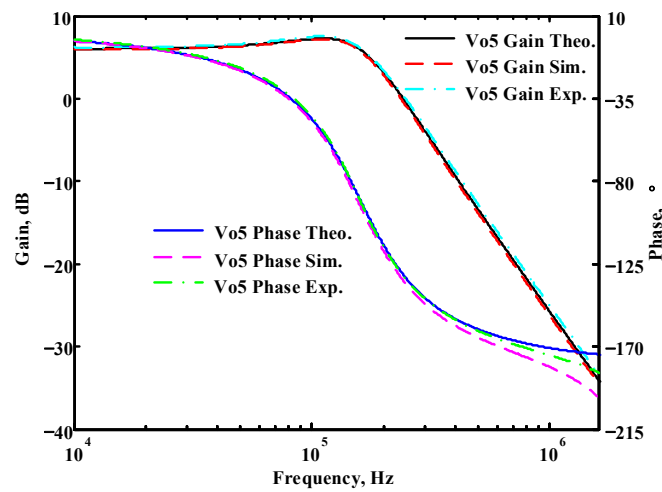


Figure 39. Simulated, measured, and theoretical comparison results of the first proposed circuit at V_{o5} .

Table 3. Frequency-domain characteristics of the pole frequency error measured at ideal pole phase for the first proposed circuit.

Output Terminal	Filter Pole Frequency			Percentage Error of the Pole Frequency	
	Theoretical	Simulated	Measured	Simulated	Measured
V_{o1}	159.15 kHz	155.59 kHz	157.2 kHz	-2.23%	-1.22%
V_{o2}	159.15 kHz	155.23 kHz	158.37 kHz	-2.46%	-0.49%
V_{o3}	159.15 kHz	155.59 kHz	157.58 kHz	-2.23%	-0.98%
V_{o4}	159.15 kHz	155.23 kHz	158.38 kHz	-2.46%	-0.48%
V_{o5}	159.15 kHz	154.88 kHz	158.76 kHz	-2.68%	-0.24%

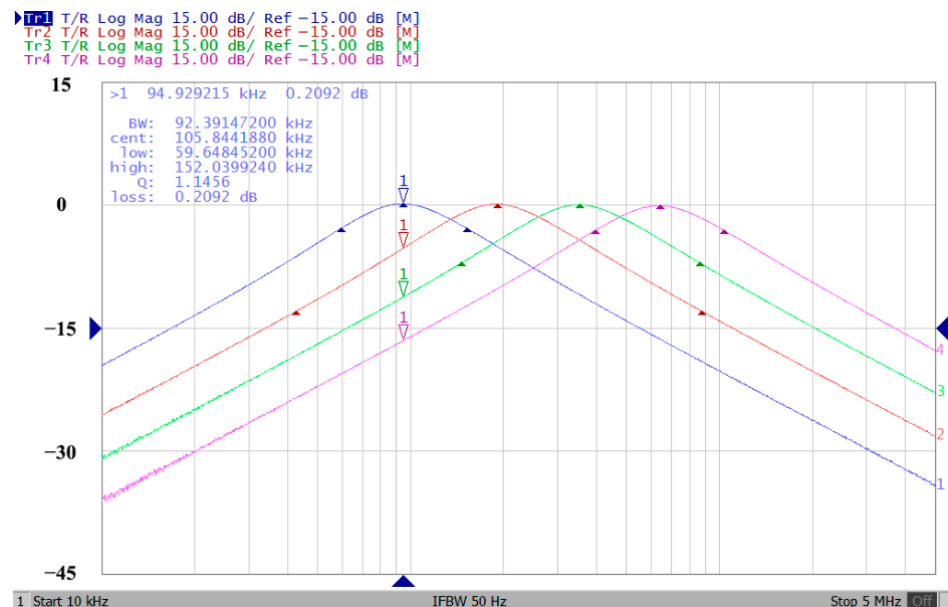


Figure 40. Electronic tunability f_0 measured at V_{o1} from 94.92 to 635.39 kHz for the first proposed circuit without affecting the Q value.

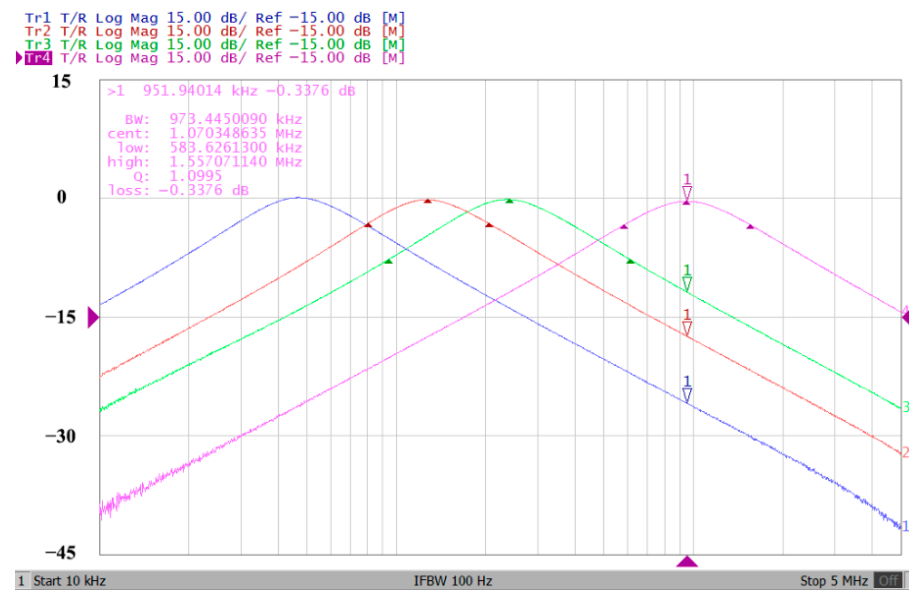


Figure 41. Electronic tunability f_0 measured at V_{O1} from 47.2 to 951.94 kHz for the first proposed circuit without affecting the Q value.

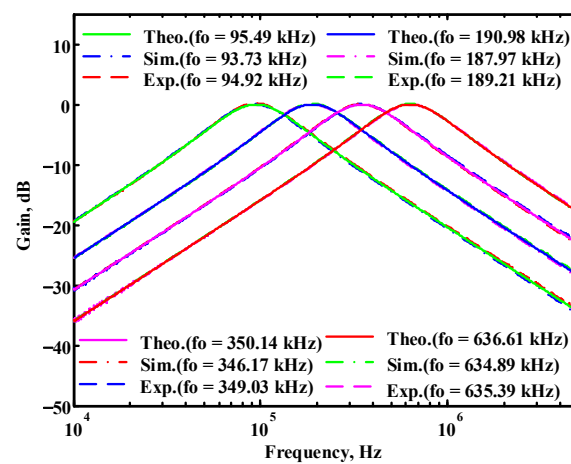


Figure 42. Simulated, measured, and theoretical comparison results of the electronic tunability f_0 at V_{O1} in Figure 40 without affecting the Q value.

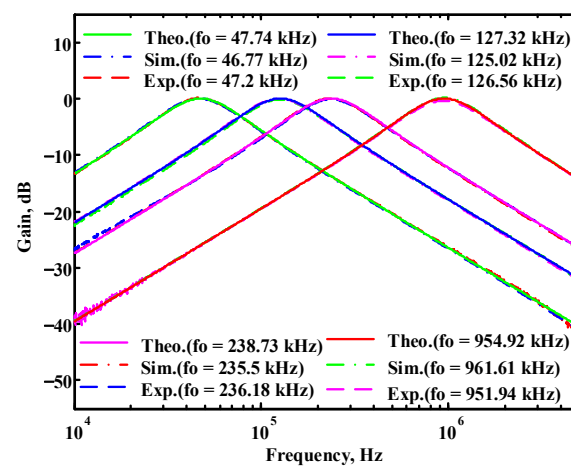


Figure 43. Simulated, measured, and theoretical comparison results of the electronic tunability f_0 at V_{O1} in Figure 41 without affecting the Q value.

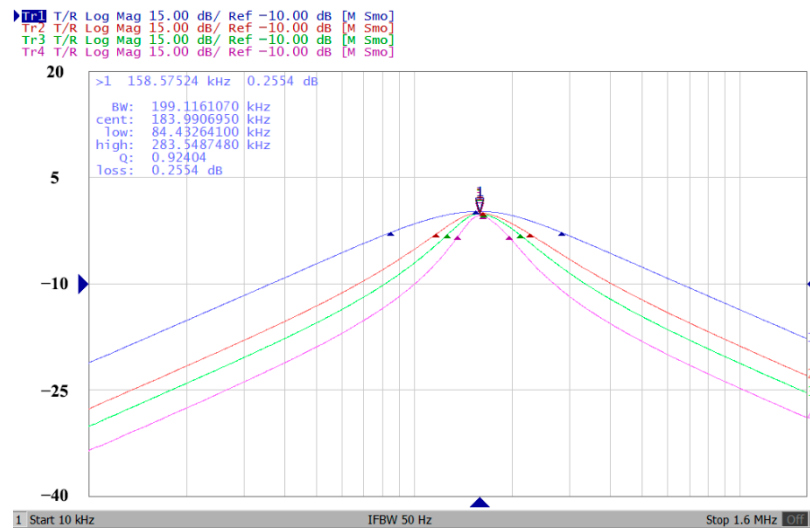


Figure 44. Measured electronic tunability Q of the first proposed circuit at V_{01} without affecting the f_0 value.

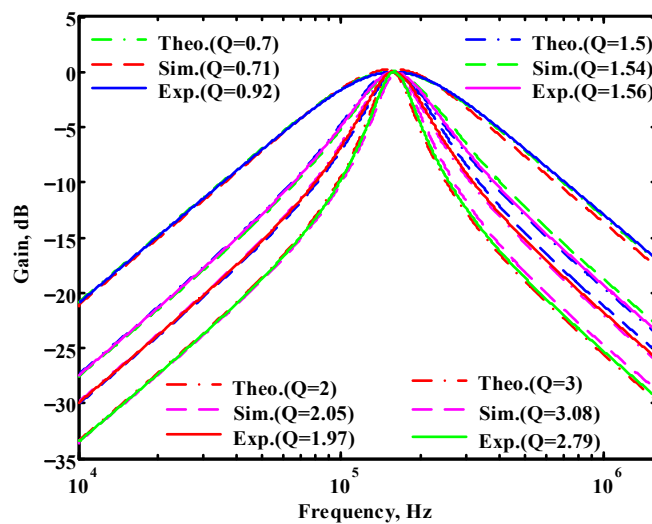


Figure 45. Simulated, measured, and theoretical comparison results of the electronic tunability Q for the first proposed circuit at V_{01} without affecting the f_0 value.

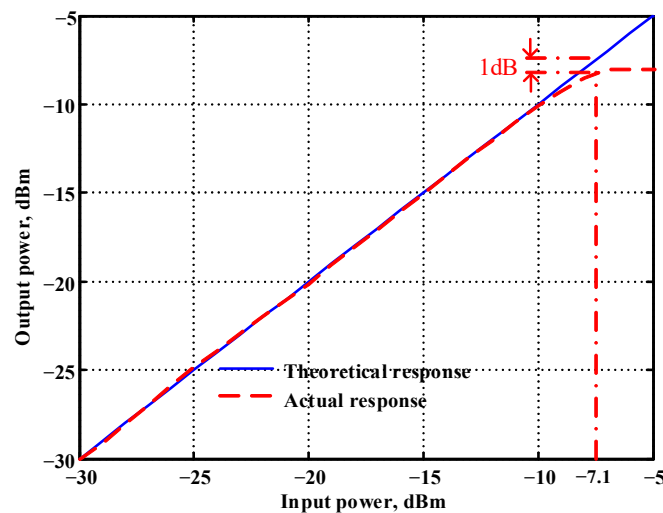


Figure 46. Measured results of the P1dB point of the first proposed circuit at V_{01} .

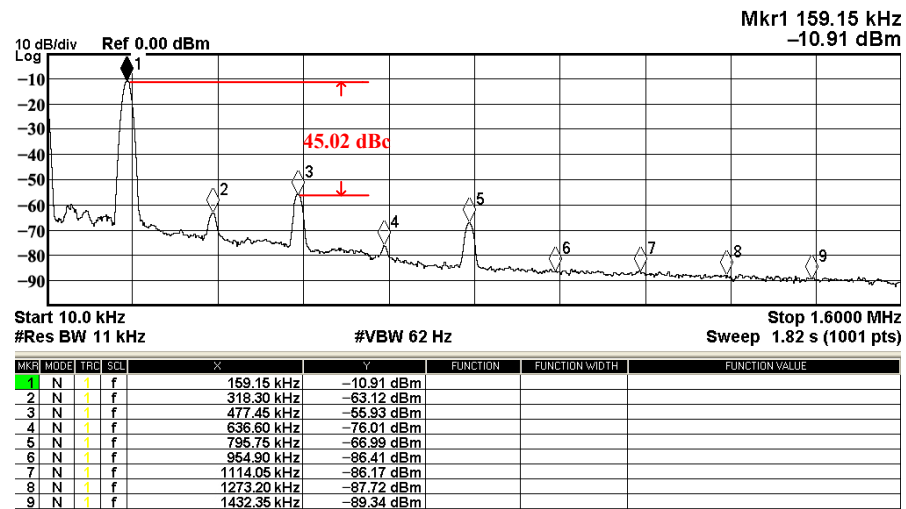


Figure 47. Measured results of the SFDR of the first proposed circuit at V_{o1} .

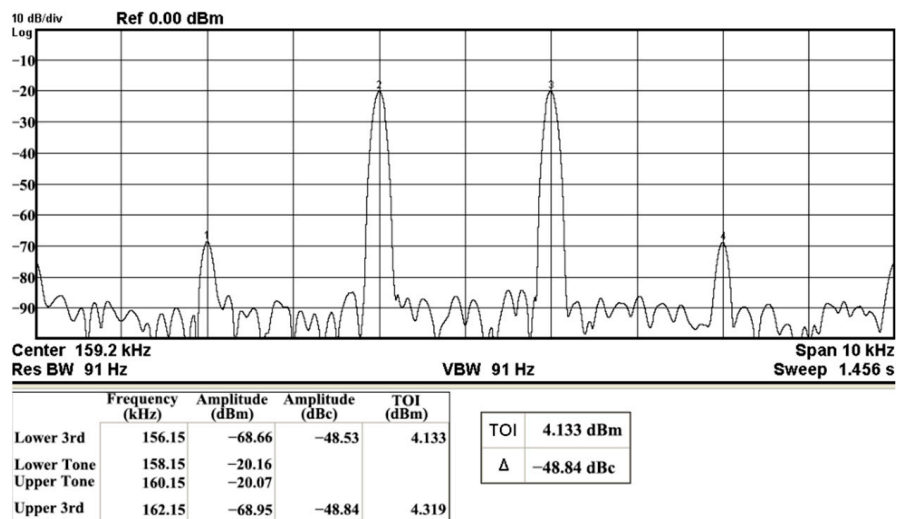


Figure 48. Measured results of the IMD of the first proposed circuit at V_{o1} .

Table 4. Summary of the measured performance of the first proposed VM LT1228-based second-order multifunction filter.

Factor							
Power Supply (V)	PD (W)	Pole Frequency (kHz)	Pole Frequency Tuning Range (kHz)	P1dB (dBm)	IMD3 (dBc)	TOI (dBm)	SFDR (dBc)
± 15	0.69	157.2	47.2–951.94	-7.1	-48.84	4.133	45.02

3.2. Verification of the Second Proposed VM LT1228-Based Multifunction Filter

To verify the operability of the second proposed VM LT1228-based multifunction filter at $f_0 = 159.15$ kHz and $Q = 1$, two capacitors $C_3 = C_4 = 1$ nF, five resistors $R = R_5 = R_6 = R_7 = R_8 = 1$ k Ω , and three commercial LT1228 ICs with bias currents of $I_{B4} = I_{B5} = I_{B6} = 100$ μ A were chosen. Figures 49–53 illustrate the simulation results of the filter magnitude and phase responses of the second proposed circuit in Figure 6. From Figures 49–53, the second proposed VM LT1228-based multifunction filter provides five output responses in the frequency-domain. Figure 54 shows that the simulation results of the Q-value can specify the recommended independent control without affecting the pole frequency. In Figure 54, the simulated Q-value varied for $Q = \{2.56, 4.06, 5.01, 5.95\}$ via the three bias currents $I_{B4} = I_{B5} = 100$ μ A and

$I_{B6} = \{40, 25, 20, 16.6\} \mu\text{A}$. This is expected since the output swing distortion limits the Q-value below 6, and the Q-value error remains below 2%. Figure 55 shows the frequency tunability results of the second proposed filter simulated at the V_{o1} output voltage. In Figure 55, the simulated pole frequency was varied for $f_o = \{46.77, 125.02, 235.5, 879.02\} \text{ kHz}$ via the three bias currents $I_{B4} = I_{B5} = \{30, 80, 150, 550\} \mu\text{A}$ and $I_{B6} = 100 \mu\text{A}$. Figures 54 and 55 confirm that the second VM multifunction filter provides electronic control of the f_o and Q parameters. Figures 56 and 57 show the frequency tunability results of the second proposed filter simulated at the V_{o2} and V_{o3} output voltages, respectively. In Figure 56, the simulated pole frequency was varied for $f_o = \{46.55, 124.16, 387.25, 849.18\} \text{ kHz}$ via the three bias currents $I_{B4} = I_{B5} = \{30, 80, 250, 550\} \mu\text{A}$ and $I_{B6} = 100 \mu\text{A}$. In Figure 57, the simulated pole frequency was varied for $f_o = \{46.66, 124.45, 389.04, 857.03\} \text{ kHz}$ via the three bias currents $I_{B4} = I_{B5} = \{30, 80, 250, 550\} \mu\text{A}$ and $I_{B6} = 100 \mu\text{A}$. To demonstrate the stability of the second proposed multifunction filter at different temperatures, the NBPF (V_{o1}), ILPF (V_{o2}), and NHPF (V_{o3}) of the second circuit are operated at different temperatures. Figures 58–60 show the NBPF, ILPF, and NHPF operating at different temperatures, respectively. From Figures 58–60, the temperature varies from -5° to 50° . The simulated NBPF varied from 174.18 kHz to 144.54 kHz, which affects the operating pole frequency of 159.15 kHz in the range of 9.44% to -9.17% . The simulated ILPF varied from 173.78 kHz to 144.21 kHz, which affects the operating pole frequency of 159.15 kHz in the range 9.19% to -9.38% . The simulated NHPF varied from 174.18 kHz to 144.54 kHz, which affects the operating pole frequency of 159.15 kHz in the range 9.44% to -9.17% . Figures 61–65 illustrate the calculated, simulated, and measured filter amplitude and phase responses of the second proposed circuit in Figure 6. Based on the ideal pole phase marked in the frequency-domain characteristics, Table 5 shows the simulated and measured pole frequency errors for the second proposed circuit. In Table 5, the maximum percentage error of the pole frequency measured in the frequency-domain is less than 1.55%. According to Figures 61–65 and Table 5, the amplitude and phase responses of the second proposed circuit were in agreement with the simulated and measured results. Figures 66 and 67 illustrate the calculated, simulated, and measured amplitude responses of the second filter at the V_{o1} output voltage. In Figure 66, the measured pole frequency was varied for $f_o = \{47.71, 127.01, 237.05, 887.34\} \text{ kHz}$ via the three bias currents $I_{B4} = I_{B5} = \{30, 80, 150, 550\} \mu\text{A}$ and $I_{B6} = 100 \mu\text{A}$. In Figure 67, the measured quality factor varied for $Q = \{0.88, 1.62, 2.05, 2.9\}$ via the three bias currents $I_{B4} = I_{B5} = 100 \mu\text{A}$ and $I_{B6} = \{142, 66.6, 50, 33.3\} \mu\text{A}$. Figures 68–72 illustrate the time-domain characteristics of the second proposed circuit when the frequency and amplitude of the input sine wave are 159.15 kHz and 180 m V_{pp} , respectively. Table 6 shows the measured phase error between the output and input waveforms at an operating pole frequency of 159.15 kHz. In Table 6, the maximum phase error measured in the time-domain at an operating pole frequency of 159.15 kHz is less than 2.55° . Figure 73 shows the spectrum of the second proposed filter measured at the V_{o1} output voltage. In Figure 73, the frequency and amplitude of the input sine wave were 159.15 kHz and 180 m V_{pp} , respectively. As shown in Figure 73, the SFDR between the first tone and the highest spur of the other levels is 45.88 dBc, and the calculated THD value is 0.6%. Figure 74 shows the THD measured at V_{o1} versus different input voltage signals. In Figure 74, the THD is below 2% when the input peak-to-peak voltage increases to 220 m V_{pp} . The P1dB performance of the second proposed circuit is measured at the V_{o1} output voltage, and the measured input P1dB point is approximately -7 dBm , as shown in Figure 75. The IMD performance of the second proposed circuit NBPF at the V_{o1} output voltage is investigated using equal-amplitude two-tone signals with frequencies $f_1 = 158.15 \text{ kHz}$ and $f_2 = 160.15 \text{ kHz}$. Figure 76 shows the IMD results in Figure 6 for the second proposed circuit NBPF at the V_{o1} output voltage. In Figure 76, the IMD3 and TOI point were measured as -49.65 dBc and 4.316 dBm , respectively. Table 7 summarizes the measured performance of the second proposed VM LT1228-based second-order multifunction filter.

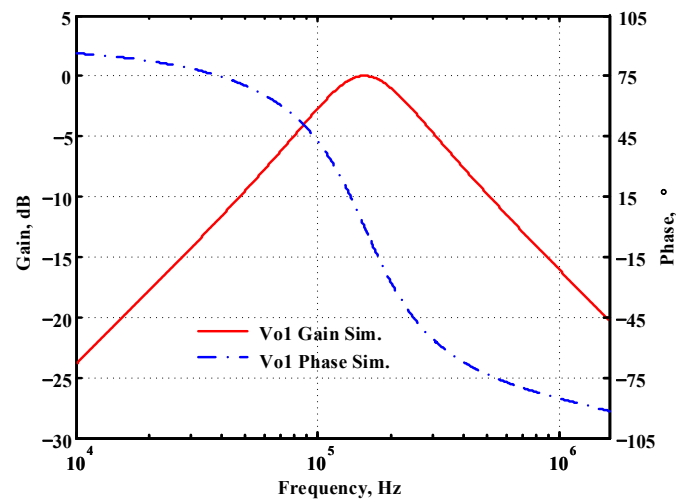


Figure 49. Simulated gain and phase frequency response of the second proposed circuit at V_{o1} .

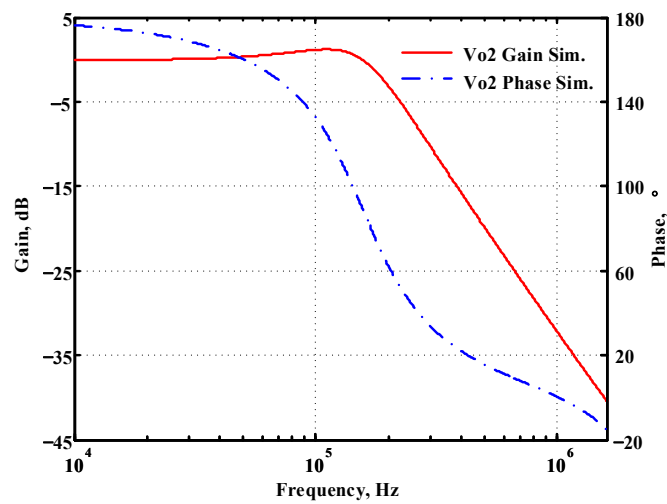


Figure 50. Simulated gain and phase frequency response of the second proposed circuit at V_{o2} .

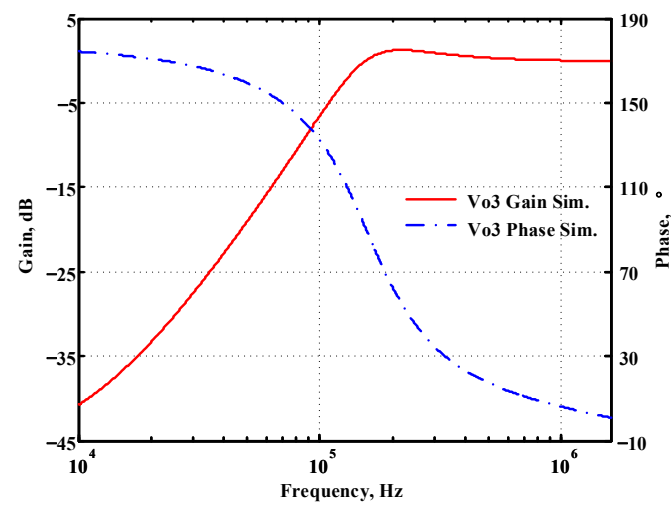


Figure 51. Simulated gain and phase frequency response of the second proposed circuit at V_{o3} .

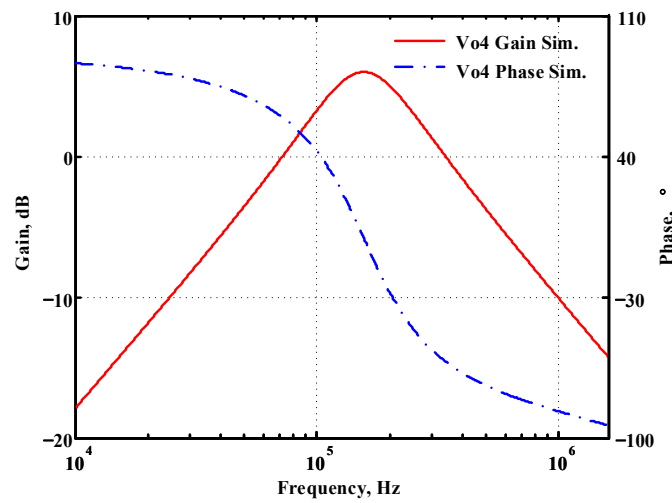


Figure 52. Simulated gain and phase frequency response of the second proposed circuit at V_{o4} .

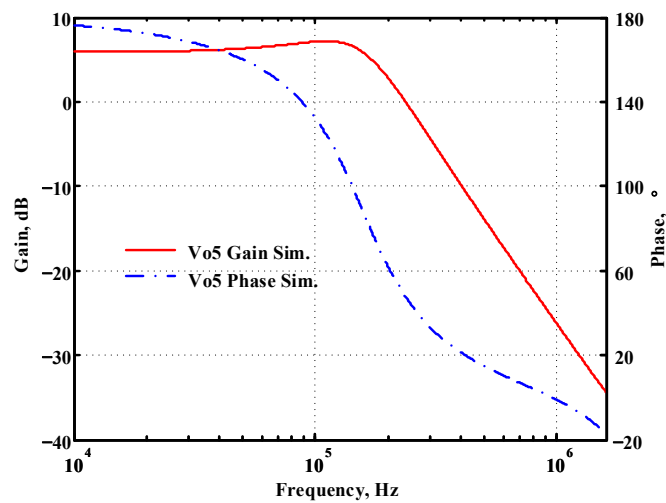


Figure 53. Simulated gain and phase frequency response of the second proposed circuit at V_{o5} .

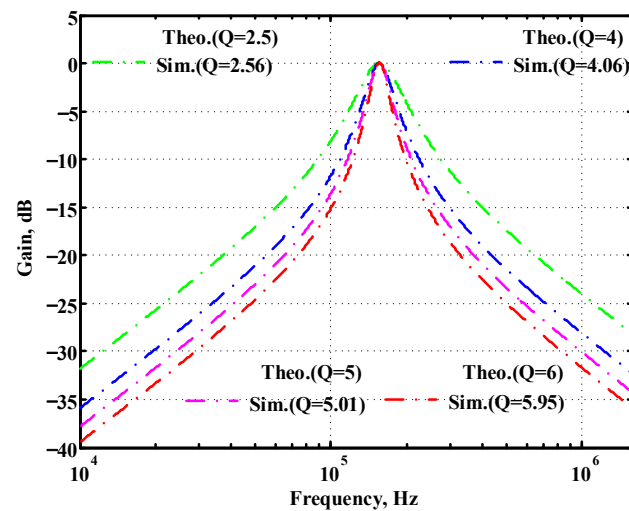


Figure 54. Simulated gain response of the second proposed circuit at V_{o1} by changing Q and keeping f_o constant.

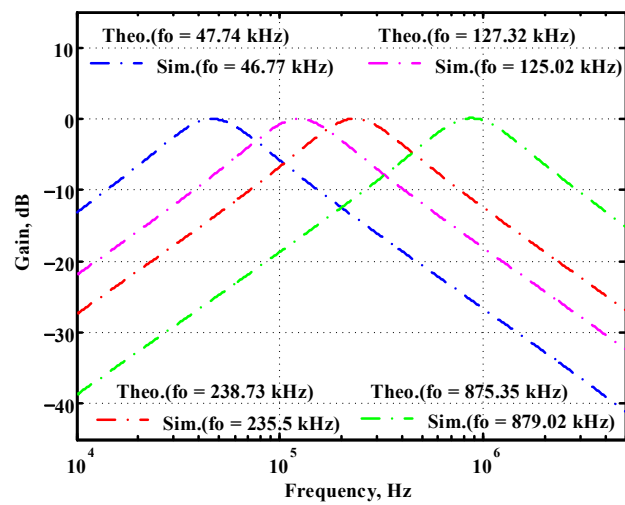


Figure 55. Simulated gain response of the second proposed circuit at V_{o1} by changing f_0 and keeping Q constant.

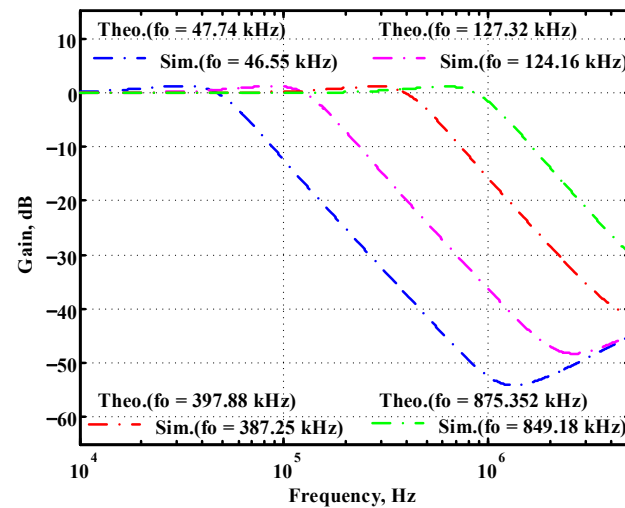


Figure 56. Simulated gain response of the second proposed circuit at V_{o2} by changing f_0 and keeping Q constant.

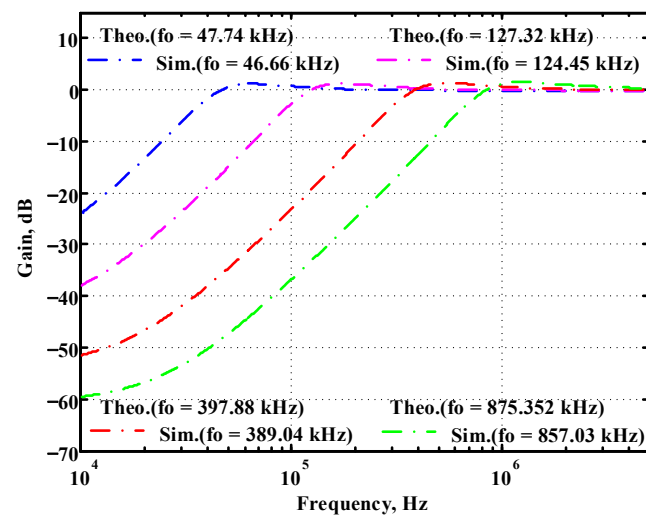


Figure 57. Simulated gain response of the second proposed circuit at V_{o3} by changing f_0 and keeping Q constant.

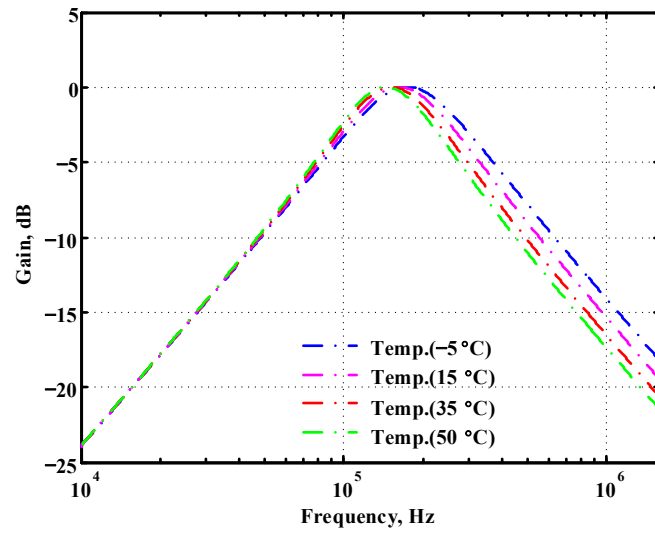


Figure 58. Simulated temperature variation at V_{O1} for the second proposed circuit.

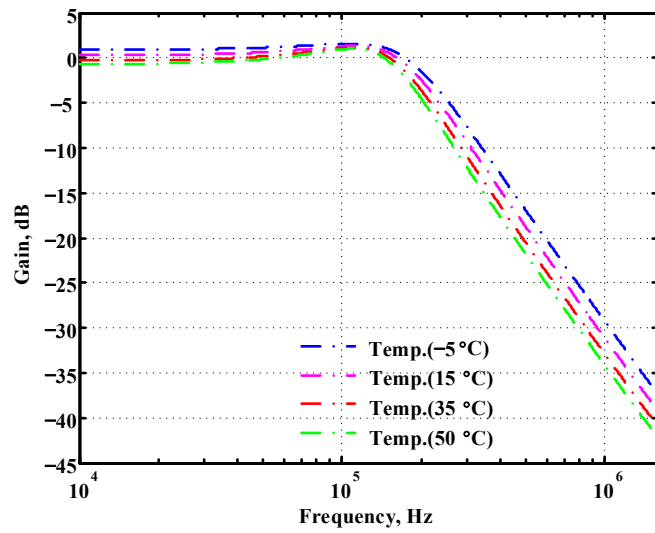


Figure 59. Simulated temperature variation at V_{O2} for the second proposed circuit.

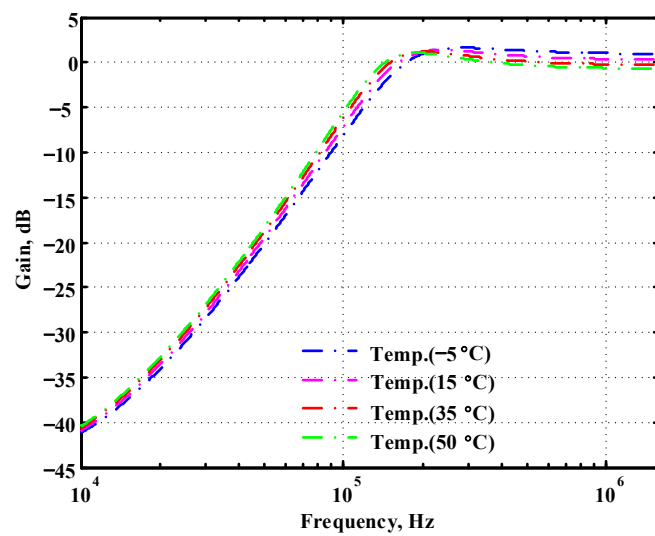


Figure 60. Simulated temperature variation at V_{O3} for the second proposed circuit.

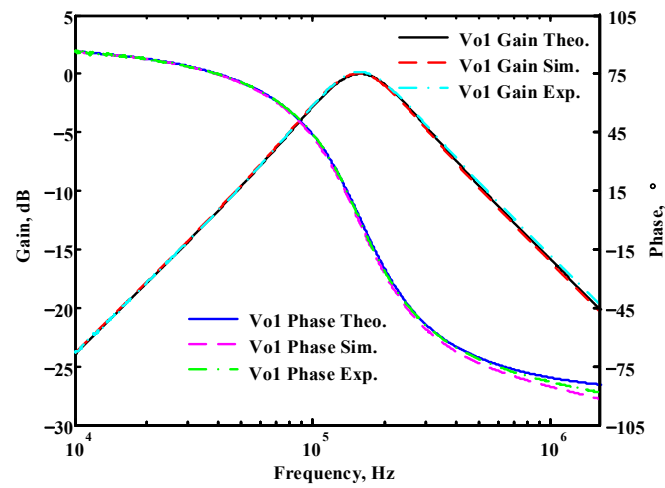


Figure 61. Simulated, measured, and theoretical comparison results of the second proposed circuit at V_{o1} .

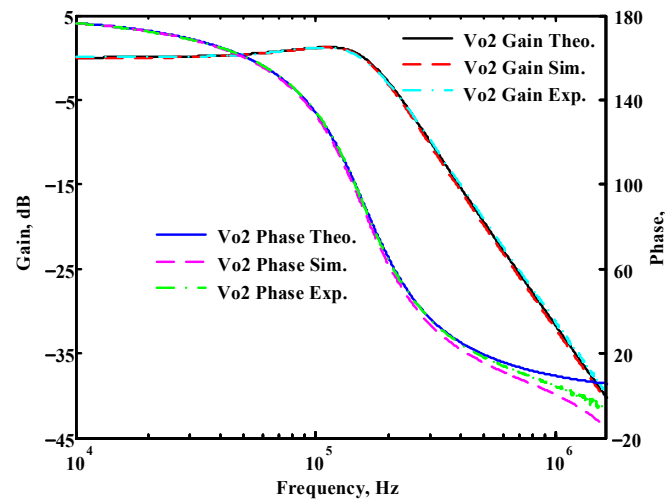


Figure 62. Simulated, measured, and theoretical comparison results of the second proposed circuit at V_{o2} .

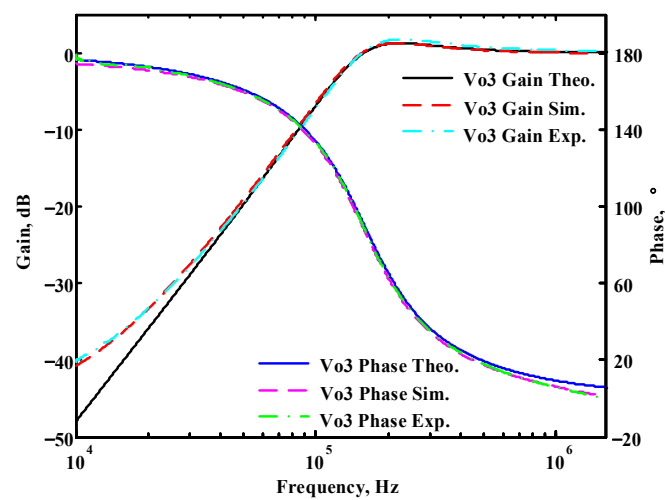


Figure 63. Simulated, measured, and theoretical comparison results of the second proposed circuit at V_{o3} .

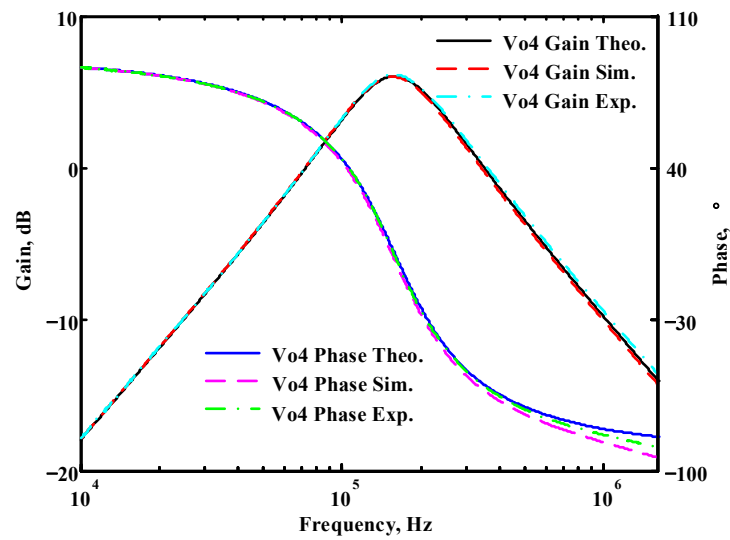


Figure 64. Simulated, measured, and theoretical comparison results of the second proposed circuit at V_{o4} .

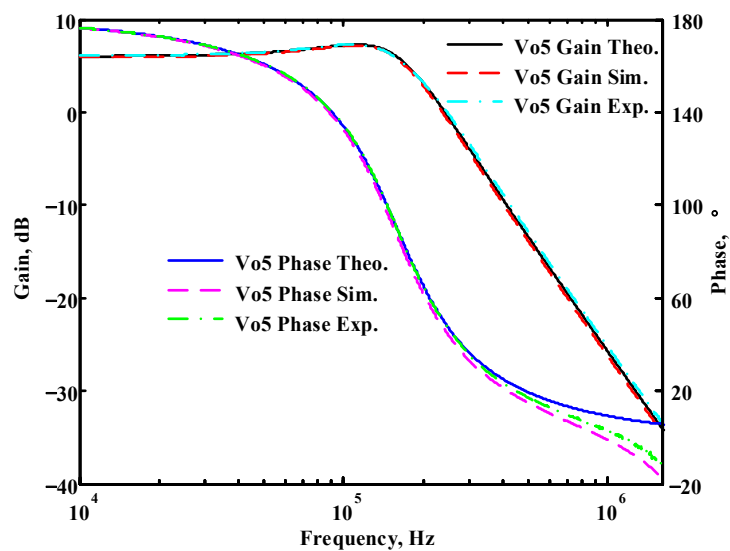


Figure 65. Simulated, measured, and theoretical comparison results of the second proposed circuit at V_{o5} .

Table 5. Frequency-domain characteristics of the pole frequency error measured at ideal pole phase for the second proposed circuit.

Output Terminal	Filter Pole Frequency			Percentage Error of the Pole Frequency	
	Theoretical	Simulated	Measured	Simulated	Measured
V_{o1}	159.15 kHz	155.59 kHz	157.55 kHz	−2.23%	−1%
V_{o2}	159.15 kHz	155.23 kHz	158.22 kHz	−2.46%	−0.58%
V_{o3}	159.15 kHz	155.59 kHz	156.67 kHz	−2.23%	−1.55%
V_{o4}	159.15 kHz	155.23 kHz	157.71 kHz	−2.46%	−0.9%
V_{o5}	159.15 kHz	154.88 kHz	158.98 kHz	−2.68%	−0.1%

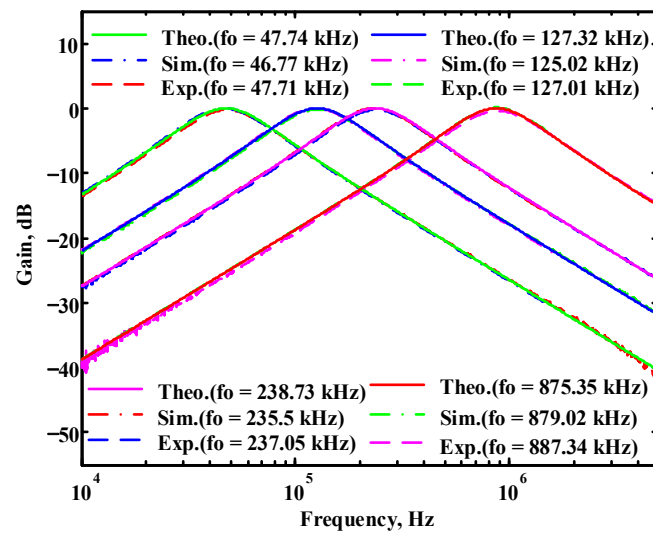


Figure 66. Simulated, measured, and theoretical comparison results of the electronic tunability f_0 for the second proposed circuit at V_{o1} without affecting the Q value.

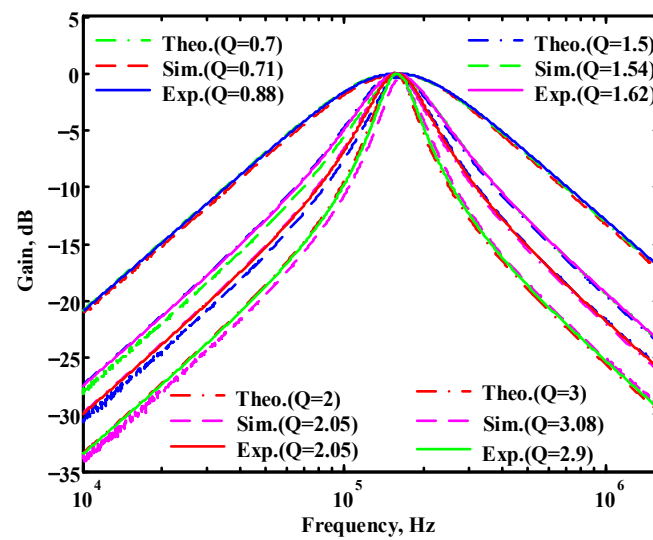


Figure 67. Simulated, measured, and theoretical comparison results of the electronic tunability Q for the second proposed circuit at V_{o1} without affecting the f_0 value.

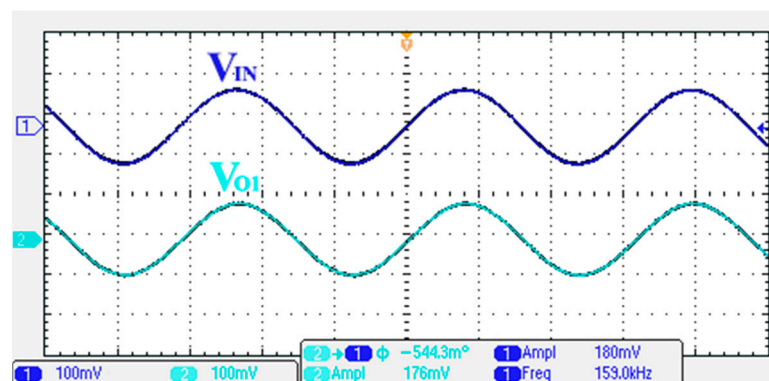


Figure 68. Measured output and input characteristics of the second proposed circuit at V_{o1} .

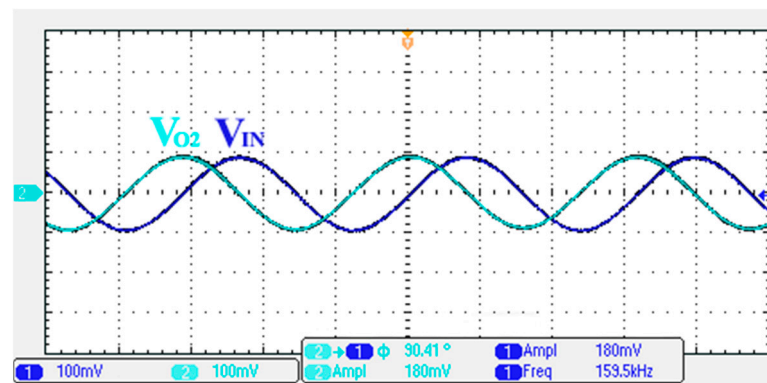


Figure 69. Measured output and input characteristics of the second proposed circuit at V_{O2} .

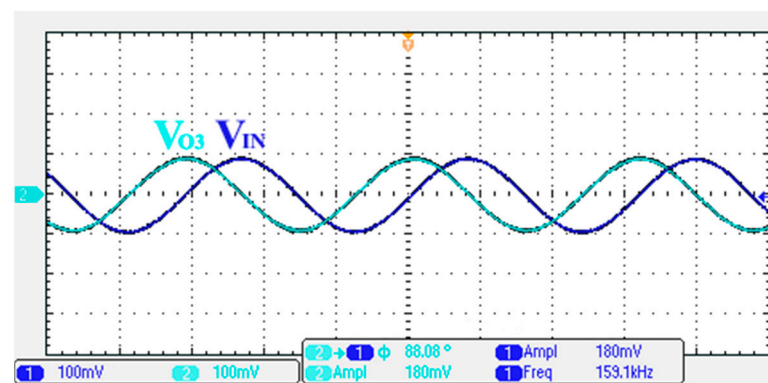


Figure 70. Measured output and input characteristics of the second proposed circuit at V_{O3} .

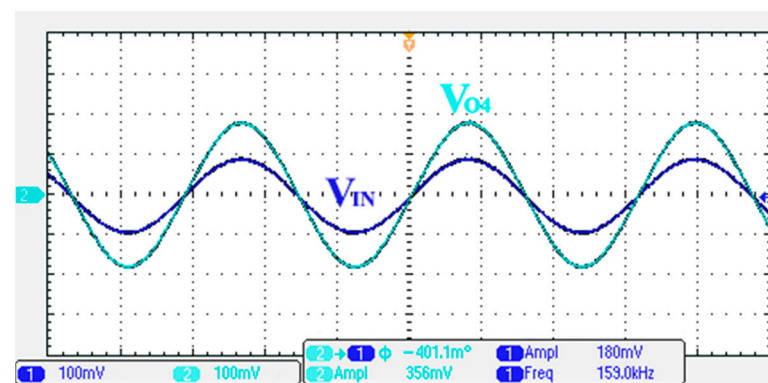


Figure 71. Measured output and input characteristics of the second proposed circuit at V_{O4} .

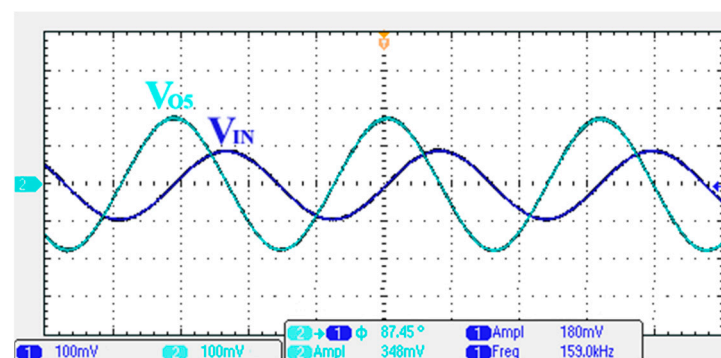


Figure 72. Measured output and input characteristics of the second proposed circuit at V_{O5} .

Table 6. Time-domain characteristics of the output phase error measured for the second proposed circuit at an operating pole frequency of 159.15 kHz.

Output Terminal	Operating Pole Phase		Output Phase Error
	Theoretical	Measured	
V _{o1}	0°	−0.544°	−0.544°
V _{o2}	90°	90.41°	0.41°
V _{o3}	90°	88.08°	−1.92°
V _{o4}	0°	−0.401°	−0.401°
V _{o5}	90°	87.45°	−2.55°

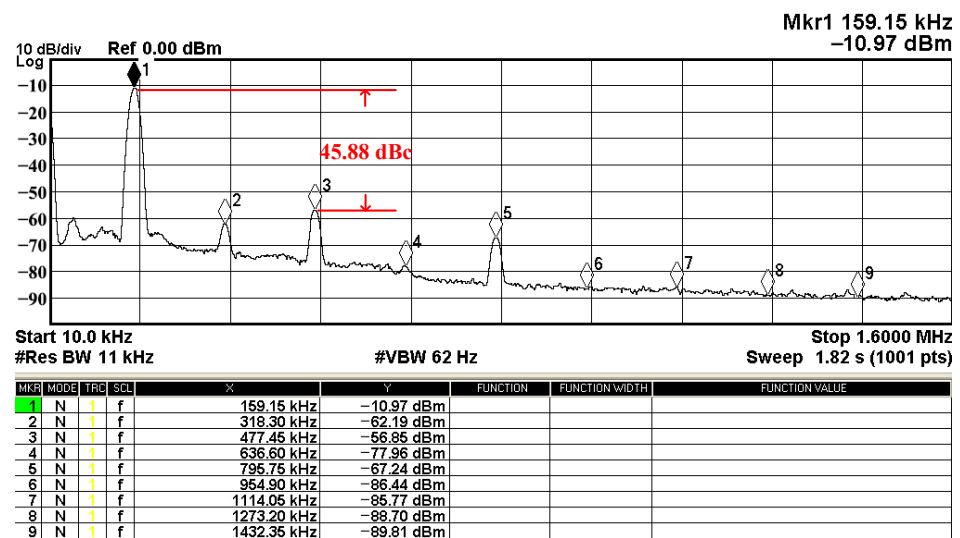


Figure 73. Measured output spectrum of Figure 68.

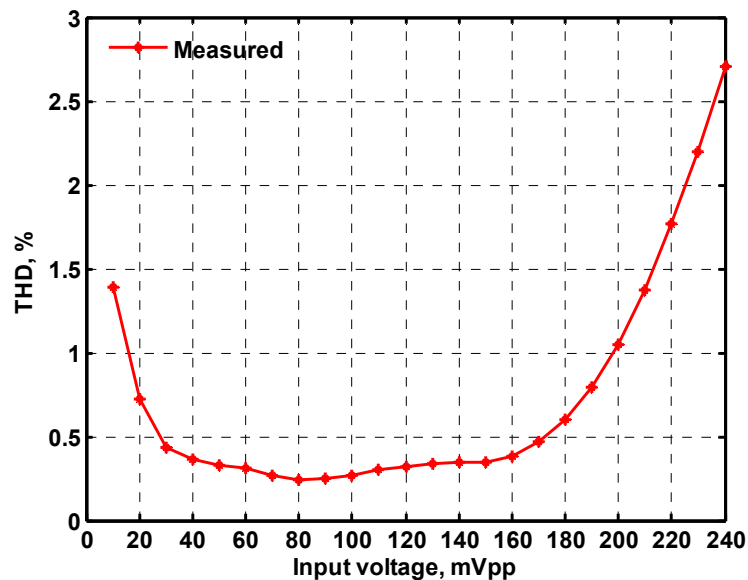


Figure 74. Measured THD of the second proposed circuit at V_{o1} in Figure 6 versus peak-to-peak input voltage signal at 159.15 kHz.

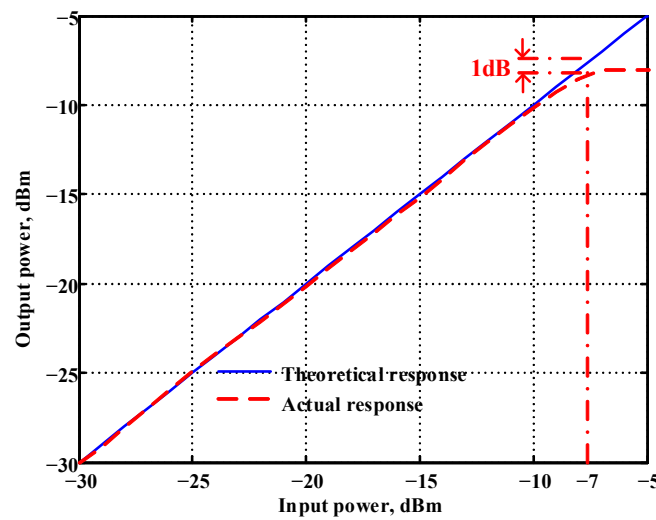


Figure 75. Measured results of the P1dB point of the second proposed circuit at V_{o1} .

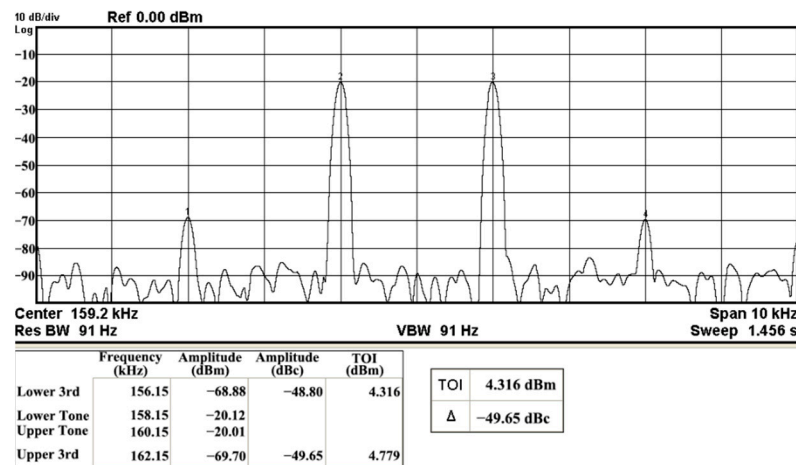


Figure 76. Measured results of the IMD3 of the second proposed circuit at V_{o1} .

Table 7. Summary of the measured performance of the second proposed VM LT1228-based second-order multifunction filter.

Factor							
Power Supply (V)	PD (W)	Pole Frequency (kHz)	Pole Frequency Tuning Range (kHz)	P1dB (dBm)	IMD3 (dBc)	TOI (dBm)	SFDR (dBc)
± 15	0.69	157.55	47.71–887.34	-7	-49.65	4.316	45.88

4. Conclusions

This paper presents the syntheses of two new VM electronically tunable one-input five-output second-order BPF, LPF, and HPF transfer functions based on three LT1228 ICs. Both configurations with a single input voltage terminal and five output voltage terminals use three commercial LT1228 ICs and seven passive components. These two newly synthesized VM second-order multifunction filters can simultaneously provide the following eight attractive advantages: (i) Both circuits can generate BPF, LPF, and HPF transfer functions simultaneously, making them suitable for use in three-way crossover networks. (ii) Both circuits have one high-impedance input, making them suitable for cascading input voltages. (iii) Both circuits have three low-impedance outputs, making them suitable for cascading three output voltages. (iv) The parameters ω_o and Q of the two filters permit electronic and orthogonal tuning. (v) The parameter Q of the two filters has independent and

electronic tuning capability. (vi) Passive components do not require matching conditions. (vii) The passband gains of the BPF and LPF responses can be controlled effectively and independently without affecting the filter parameters ω_0 and Q . (viii) Synthesis method of the electronically tunable VM second-order multifunction filter topologies based on the non-inverting/inverting HPF second-order transfer functions. Circuit design and implementation results were obtained to demonstrate these two VM LT1228-based second-order multifunction filters. The measured input P1dB, IMD3, TOI, and SFDR of the first filter were -7.1 dBm, -48.84 dBc, 4.133 dBm, and 45.02 dBc, respectively. The measured input P1dB, IMD3, TOI, and SFDR of the second filter were -7 dBm, -49.65 dBc, 4.316 dBm, and 45.88 dBc, respectively. Both circuits use a topology synthesis method based on the VM second-order non-inverting/inverting HP filter transfer functions to generate the BP, LP, and HP filter transfer functions simultaneously, making them suitable for three-way crossover network high-fidelity loudspeaker applications. Three commercial LT1228 ICs and seven passive components were used in OrCAD PSpice simulations and experimental measurements to verify the operation of the two proposed VM LT1228-based second-order multifunction filter topologies.

Author Contributions: Methodology and writing—original draft preparation H.-P.C.; formal analysis and investigation, H.-P.C., S.-J.C. and C.-Y.C.; Software, S.-J.C. and C.-Y.C.; Validation, H.-P.C., S.-J.C. and C.-Y.C. All authors have read and agreed to the published version of the manuscript.

Funding: This research received no external funding.

Institutional Review Board Statement: Not applicable

Informed Consent Statement: Not applicable.

Data Availability Statement: Not applicable.

Conflicts of Interest: The authors declare no conflict of interest.

References

1. Kumngern, M.; Aupithak, N.; Khateb, F.; Kulej, T. 0.5 V Fifth-order butterworth low-pass filter using multiple-input OTA for ECG applications. *Sensors* **2020**, *20*, 7343. [[CrossRef](#)] [[PubMed](#)]
2. Prommee, P.; Wongprommoon, N.; Kumngern, M.; Jaikla, W. Low-voltage low-pass and band-pass elliptic filters based on log-domain approach suitable for biosensors. *Sensors* **2019**, *19*, 5581. [[CrossRef](#)] [[PubMed](#)]
3. Sotner, R.; Jerabek, J.; Polak, L.; Theumer, R.; Langhammer, L. Electronic tunability and cancellation of serial losses in wire coils. *Sensors* **2022**, *22*, 7373. [[CrossRef](#)] [[PubMed](#)]
4. Márquez, A.; Pérez-Bailón, J.; Calvo, B.; Medrano, N.; Martínez, P.A. A CMOS self-contained quadrature signal generator for SoC impedance spectroscopy. *Sensors* **2018**, *18*, 1382. [[CrossRef](#)]
5. Zhao, Z.; Tong, H.; Deng, Y.; Xu, W.; Zhang, Y.; Ye, H. Single-lead fetal ECG extraction based on a parallel marginalized particle filter. *Sensors* **2017**, *17*, 1456. [[CrossRef](#)]
6. Akbari, M.; Hussein, S.M.; Hashim, Y.; Tang, K.T. An adjustable dual-output current mode MOSFET-only filter. *IEEE Trans. Circuits Syst. II Exp. Briefs* **2021**, *68*, 1817–1821. [[CrossRef](#)]
7. Alpaslan, H.; Yuce, E. DVCC+ based multifunction and universal filters with the high input impedance features. *Analog. Integr. Circuits Signal Processing* **2020**, *103*, 325–335. [[CrossRef](#)]
8. Jaikla, W.; Khateb, F.; Kulej, T.; Pitaksuttayaprot, K. Universal filter based on compact CMOS structure of VDDDA. *Sensors* **2021**, *21*, 1683. [[CrossRef](#)]
9. Abaci, A.; Alpaslan, H.; Yuce, E. First-order all-pass filters comprising one modified DDCC. *J. Circuits Syst. Comput.* **2022**, *31*, 2250184. [[CrossRef](#)]
10. Supavarasuwat, P.; Kumngern, M.; Sangyaem, S.; Jaikla, W.; Khateb, F. Cascadable independently and electronically tunable voltage-mode universal filter with grounded passive components. *AEU Int. J. Electron. Commun.* **2018**, *84*, 290–299. [[CrossRef](#)]
11. Yuce, E.; Verma, R.; Pandey, N.; Minaei, S. New CFOA-based first-order all-pass filters and their applications. *AEU Int. J. Electron. Commun.* **2019**, *103*, 57–63. [[CrossRef](#)]
12. Unuk, T.; Yuce, E. A mixed-mode filter with DVCCs and grounded passive components only. *Int. J. Electron. Commun.* **2022**, *144*, 154063. [[CrossRef](#)]
13. Arora, T.S.; Singh, A.K. A new voltage mode sinusoidal quadrature oscillator employing second generation voltage conveyor. *Int. J. Electron. Commun.* **2022**, *154*, 154304. [[CrossRef](#)]
14. Yucehan, T.; Yuce, E. CCII-based voltage-mode and current-mode high-order filters with gains and grounded passive elements only. *Int. J. Electron. Commun.* **2022**, *155*, 154346. [[CrossRef](#)]

15. Raj, A.; Bhaskar, D.R.; Senani, R.; Kumar, P. Extension of recently proposed two-CFOA-GC all pass filters to the realisation of first order universal active filters. *Int. J. Electron. Commun.* **2022**, *146*, 154119. [CrossRef]
16. Tseng, S.Y.; Wu, R.B. Synthesis of chebyshev/elliptic filters using minimum acoustic wave resonators. *IEEE Access* **2019**, *7*, 103456–103462. [CrossRef]
17. Prommee, P.; Karawanich, K.; Khateb, F.; Kulej, T. Voltage-mode elliptic band-pass filter based on multiple-input transconductor. *IEEE Access* **2021**, *9*, 32582–32590. [CrossRef]
18. Kumngern, M.; Khateb, F.; Kulej, T.; Psychalions, C. Multiple-input universal filter and quadrature oscillator using multiple-input operational transconductance amplifiers. *IEEE Access* **2021**, *9*, 56253–56263. [CrossRef]
19. Khateb, F.; Kumngern, M.; Kulej, T.; Biolek, D. 0.5 V differential difference transconductance amplifier and its application in voltage-mode universal filter. *IEEE Access* **2022**, *10*, 43209–43220. [CrossRef]
20. Chen, H.P.; Wang, S.F.; Ku, Y.; Yi, Y.C.; Li, Y.F.; Chen, Y.H. Four unity/variable gain first-order cascaded voltage-mode all-pass filters and their fully uncoupled quadrature sinusoidal oscillator applications. *Sensors* **2022**, *22*, 6250. [CrossRef]
21. Horng, J.W.; Hou, C.L.; Chang, C.M.; Chung, W.Y. Voltage-mode universal biquadratic filters with one input and five outputs. *Analog Integr. Circuits Signal Processing* **2006**, *47*, 73–83. [CrossRef]
22. Horng, J.W.; Chiu, W.Y. High input impedance voltage-mode biquad with one input and five outputs employing four CCII ICs. *Indian J. Pure Appl. Phys.* **2016**, *54*, 577–582.
23. Wang, S.F.; Chen, H.P.; Ku, Y.; Zhong, M.X. Voltage-mode multifunction biquad filter and its application as fully-uncoupled quadrature oscillator based on current-feedback operational amplifiers. *Sensors* **2020**, *20*, 6681. [CrossRef] [PubMed]
24. Wang, S.F.; Chen, H.P.; Ku, Y.; Zhong, M.X. Analytical synthesis of high-pass, band-pass and low-pass biquadratic filters and its quadrature oscillator application using current-feedback operational amplifiers. *IEEE Access* **2021**, *9*, 13330–13343. [CrossRef]
25. Bhaskar, D.R.; Raj, A.; Senani, R. Three new CFOA-based SIMO-type universal active filter configurations with unrivalled features. *AEU Int. J. Electron. Commun.* **2022**, *153*, 154285. [CrossRef]
26. Tuntrakool, S.; Kumngern, M.; Sotner, R.; Herencsar, N.; Suwanjan, P.; Jaikla, W. High input impedance voltage-mode universal filter and its modification as quadrature oscillator using VDDAs. *Indian J. Pure Appl. Phys.* **2017**, *55*, 324–332.
27. Huaihongthong, P.; Chaichana, A.; Suwanjan, P.; Siripongdee, S.; Sunthonkanokpong, W.; Supavarasuwat, P.; Jaikla, W.; Khateb, F. Single-input multiple-output voltage-mode shadow filter based on VDDAs. *AEU Int. J. Electron. Commun.* **2019**, *103*, 13–23. [CrossRef]
28. Jaikla, W.; Siripongdee, S.; Khateb, F.; Sotner, R.; Silapan, P.; Suwanjan, P.; Chaichana, A. Synthesis of biquad filters using two VD-DIBAs with independent control of quality factor and natural frequency. *AEU Int. J. Electron. Commun.* **2021**, *132*, 153601. [CrossRef]
29. Wang, S.F.; Chen, H.P.; Ku, Y.; Lin, Y.C. Versatile tunable voltage-mode biquadratic filter and its application in quadrature oscillator. *Sensors* **2019**, *19*, 2349. [CrossRef]
30. Wang, S.F.; Chen, H.P.; Ku, Y.; Yang, C.M. Independently tunable voltage-mode OTA-C biquadratic filter with five inputs and three outputs and its fully-uncoupled quadrature sinusoidal oscillator application. *AEU Int. J. Electron. Commun.* **2019**, *110*, 152822. [CrossRef]
31. Wang, S.F.; Chen, H.P.; Ku, Y.; Lee, C.L. Versatile voltage-mode biquadratic filter and quadrature oscillator using four OTAs and two grounded capacitors. *Electronics* **2020**, *9*, 1493. [CrossRef]
32. Wang, S.F.; Chen, H.P.; Ku, Y.; Chen, W.Y. Isomorphic circuits of independent amplitude tunable voltage-mode bandpass filters and quadrature sinusoidal oscillators. *Appl. Sci.* **2021**, *11*, 7431. [CrossRef]
33. Wai, M.P.P.; Suwanjan, P.; Jaikla, W.; Chaichana, A. Electronically and orthogonally tunable SITO voltage-mode multifunction biquad filter using LT1228s. *Elektron. Elektrotehnika* **2021**, *27*, 11–17. [CrossRef]
34. Wai, M.P.P.; Jaikla, W.; Suwanjan, P.; Sunthonkanokpong, W. Single input multiple output voltage mode universal filters with electronic controllability using commercially available ICs. In Proceedings of the 2020 17th International Conference on Electrical Engineering/Electronics, Computer, Telecommunications and Information Technology (ECTI-CON), Phuket, Thailand, 24–27 June 2020; pp. 607–610. Available online: <https://ieeexplore.ieee.org/document/9158223> (accessed on 4 August 2020).
35. Wai, M.P.P.; Chaichana, A.; Jaikla, W.; Siripongdee, S.; Suwanjan, P. One input voltage and three output voltage universal biquad filters with orthogonal tune of frequency and bandwidth. *Int. J. Electr. Comput. Eng.* **2021**, *11*, 2962–2973.
36. Olsak, M.; Vrba, K.; Matejcek, L. Electronically tunable high-order highpass filters with minimum of components. *Electr. Eng.* **2003**, *54*, 57–62.
37. Siripongdee, S.; Jaikla, W. Electronically controllable grounded inductance simulators using single commercially available IC: LT1228. *AEU-Int. J. Electron. Commun.* **2017**, *76*, 1–10. [CrossRef]
38. Siripongdee, S.; Jaikla, W. Universal filter using single commercially available IC: LT1228. In Proceedings of the 2016 the 3rd International Conference on Mechatronics and Mechanical Engineering, (MATEC Web Conf.), Kuala Lumpur, Malaysia, 28–30 November 2017; Volume 95, p. 14022. Available online: https://www.matec-conferences.org/articles/mateconf/abs/2017/09/mateconf_icmme2017_14002/mateconf_icmme2017_14002.html (accessed on 9 February 2017).
39. Rungsa, S.; Jantakun, A. Single commercially available IC: LT1228 based sinusoidal oscillator. *Przełąd Elektrotechniczny* **2019**, *95*, 218–222. [CrossRef]

40. Suwanjan, P.; Siripongdee, S.; Jaikla, W. Three-inputs single-output voltage-mode universal filter with orthogonal control using single commercially available IC. In Proceedings of the 2017 European Conference on Electrical Engineering and Computer Science (EECS), Bern, Switzerland, 17–19 November 2017; pp. 454–457. Available online: <https://ieeexplore.ieee.org/document/8412066> (accessed on 19 July 2018).
41. Klungtong, S.; Thanapatay, D.; Jaikla, W. Three-input single-output voltage-mode multifunction filter with electronic controllability based on single commercially available IC. *Act. Passiv. Electron. Compon.* **2017**, *2017*, 5240751. [[CrossRef](#)]
42. Chaichana, A.; Siripongdee, S.; Jaikla, W. Electronically adjustable voltage-mode first-order allpass filter using single commercially available IC. In Proceedings of the 2019 International Conference on Smart Materials Applications (ICSMA), Tokyo, Japan, 19–22 January 2019; pp. 19–22. Available online: <https://iopscience.iop.org/article/10.1088/1757-899X/559/1/012009> (accessed on 1 June 2019).
43. Roongmuanpha, N.; Suesut, T.; Tangsrirat, W. Electronically tunable triple-input single-output voltage-mode biquadratic filter implemented with single integrated circuit package. *Adv. Sci. Technol. Eng. Syst. J.* **2021**, *6*, 1120–1127. Available online: <https://www.astesj.com/v06/i01/p125/> (accessed on 25 February 2021). [[CrossRef](#)]
44. Onanong, N.; Supavarasuwat, P.; Angamnuaysiri, D.; Siripongdee, S.; Chaichana, A.; Jaikla, W.; Suwanjan, P. Design of electronically controllable multifunction active filter with amplitude controllability using two commercially available ICs. *J. Electr. Comput. Eng.* **2022**, *2022*, 4932284. [[CrossRef](#)]
45. Angkun, K.; Kaewon, R.; Silapan, P. A square wave and sinusoidal quadrature oscillator based-on LT1228. In Proceedings of the 2021 18th International Conference on Electrical Engineering/Electronics, Computer, Telecommunications and Information Technology (ECTI-CON), Chiang Mai, Thailand, 19–22 May 2021; pp. 833–836. Available online: <https://ieeexplore.ieee.org/document/9454933> (accessed on 18 June 2021).
46. Singh, G.; Garima. Universal biquad fractional order filter using single LT1228 IC. In Proceedings of the 2020 IEEE International Conference for Innovation in Technology (INOCON), Bangluru, India, 6–8 November 2020; pp. 1–6. Available online: <https://ieeexplore.ieee.org/document/9298397> (accessed on 1 January 2021).
47. Thanyaratsakul, N.; Tanthong, A.; Tritummanurak, T.; Keawon, R.; Paponpen, K.; Silapan, P.; Jaikla, W. Single LT1228 based electronically controllable sawtooth generator. In Proceedings of the 2021 9th International Electrical Engineering Congress (iEECON), Pattaya, Thailand, 10–12 March 2021; pp. 349–352. Available online: <https://ieeexplore.ieee.org/document/9440332> (accessed on 31 May 2021).
48. Silapan, P.; Choykhuntod, P.; Kaewon, R.; Jaikla, W. Duty-cycle electronically tunable triangular/square wave generator using LT1228 commercially available ICs for capacitive sensor interfacing. *Sensors* **2022**, *22*, 4922. [[CrossRef](#)]
49. Linear Technology Corporation. LT1228—100 MHz Current Feedback Amplifier with DC Gain Control, Linear Technology Corporation Version Number D. 2012. Available online: <http://www.linear.com/product/LT1228> (accessed on 12 May 2019).